A&A 384, 743–762 (2002)
DOI: 10.1051/0004-6361:20011779

Astronomy & Astrophysics

Weak lensing analysis of MS 1008–1224 with the VLT⋆

R. M. Athreya[1,5,6], Y. Mellier[1,2], L. van Waerbeke[3], R. Pelló[4], B. Fort[1], and M. Dantel-Fort[2]

[1] Institut d'Astrophysique de Paris, 98bis boulevard Arago, 75014 Paris, France
[2] Observatoire de Paris, DEMIRM, 61 Av. de l'Observatoire, 75014 Paris, France
[3] Canadian Institute for Theoretical Astrophysics, 60 St George Str., Toronto, M5S 3H8, Canada
[4] Observatoire Midi-Pyrénées, UMR 5572, 14 avenue Édouard Belin, 31400 Toulouse, France
[5] European Southern Observatory, Alonso de Cordova 3107, Vitacura, Casilla 19001, Santiago, Chile
[6] Departamento de Astronomia y Astrofisica, Pontificia Universidad Catolica, Casilla 104, Santiago 22, Chile

Received 4 October 1999 / Accepted 5 December 2001

Abstract. We present a gravitational lensing analysis of the cluster of galaxies MS 1008–1224 ($z = 0.31$), based on very deep observations obtained using the VLT with FORS1 and ISAAC during the science verification phase. Two different mass reconstruction algorithms were applied to the B-, V-, R- and I-band data to obtain similar projected mass distributions in all the bands. The FORS1 (BVRI) and ISAAC (JK) data were combined to determine the photometric redshift distribution of galaxies within the ISAAC field and to estimate the mass. We inferred from weak shear a minimum mass of $2.3 \times 10^{14}\ h^{-1}\ M_{\odot}$ on large scales (within $\sim$700 h^{-1} kpc, diameter) which agrees well with the X-ray mass mass estimate. The Mass-to-light ratios are also in excellent agreement. The observed mass profile is consistent with Pseudo-Isothermal Sphere models as well as a Navarro, Frenk and White model. In the inner regions the lensing mass is about twice as high as the X-ray mass which supports the long-held view that complex physical processes occuring in the innermost parts of lensing-clusters are mainly responsible for the X-ray-lensing mass discrepancy. We found that the central part of the cluster comprises two mass peaks whose center of mass is located 10–20 arcsec north of the cD galaxy. A similar offset between the cD and the peak of the X-ray distribution has been reported before. The optical, X-ray and the mass distributions show that MS 1008–1224 is composed of several subsystems which are probably undergoing a merger. It is likely that the gas is not in equilibrium in the innermost regions which vitiates the X-ray mass estimate there. We discovered that MS 1008–1224 shows a remarkable case of cluster-cluster lensing. The photometric redshifts show an excess of galaxies located 30 arcsec south-west of the cD galaxy at a redshift of $\sim$0.9. This distant cluster is therefore also lensed by MS 1008–1224, which, if confirmed with spectroscopic data, would make this the first known case of magnification of a distant cluster by another one.

Key words. cosmology: dark matter – gravitational lensing – galaxies: clusters: individual: MS 1008–1224

1. Introduction

The analysis of the distribution of dark matter in clusters of galaxies provides an important insight into the history of structure formation in the Universe. Their epoch of formation and their evolution with redshift are dependent on cosmological parameters and the nature of (dark) matter. In particular, it is widely believed that the existence of even a few massive clusters at redshift $z \approx 1$ will be a strong indicator of a low mass density universe (e.g. Bahcall et al. 1997).

It is essential that we develop reliable tools to probe the amount and distribution of each matter component and follow their evolution with redshift. Gravitational lensing and bremsstrahlung emission from hot intracluster gas are two processes which help us in addressing these issues. Unfortunately, the results from these two approaches have not always been consistent with each other.

Indeed, X-ray mass estimates show discrepancies with weak- and strong-lensing mass estimates of clusters of galaxies. The reasons for the discrepancy are not yet fully understood (see Mellier 1999 for a review). The total mass inferred from lensing exceeds the X-ray mass by a factor of about two for some clusters including well studied ones like A2218 (Miralda-Escudé & Babul 1995). Investigations of a dozen clusters by Smail et al. (1997), Allen (1998) and Lewis et al. (1999) have not provided conclusive answers. Allen (1998) compared cooling flow and non-cooling flow clusters and observed that the former do not show the mass discrepancy. This result suggests that the

Send offprint requests to: Y. Mellier, e-mail: mellier@iap.fr

⋆ Based on observations obtained at the Very Large Telescope at Cerro Paranal operated by the European Southern Observatory.

assumptions regarding the dynamical and thermal state of the hot intra-cluster gas, a key ingredient for the X-ray mass estimate, are not realistic enough for a satisfactory model of non-cooling flow (i.e. presumably non-relaxed) clusters of galaxies. This interpretation was reinforced by Böhringer et al. (2000) and Allen et al. (2001) who found an excellent agreement between the X-ray data from ROSAT and Chandra and the strong- and weak-lensing analyses of the relaxed cluster A2390. However, Lewis et al. (1999) found significant discrepancies even in some cooling flow clusters between the X-ray and lensing mass, particularly with strong-lensing estimates.

It is likely that this mass discrepancy is the result of several less-than-valid assumptions. For example, the comparison between X-ray and weak gravitational lensing is done by extrapolating the best fit of the X-ray profile far beyond the region where data are reliable, where uncertainties are obviously significant and the shape of the (assumed) analytical profile used for extrapolation has a considerable impact on the mass estimate (Lewis et al. 1999; Böhringer et al. 1999).

Lensing mass estimates are not free from bias either. N-body simulations by Cen (1997) and Metzler et al. (1999) show that projection effects of in-falling filaments of matter towards the cluster centre can significantly bias the projected mass density inferred from weak lensing analysis to values higher than those derived from X-ray. Estimates of the bias are typically between 10 and 20 per cent but projection effects due to structures along the line of sight can overestimate the total mass by about 30 per cent (Reblinsky & Bartelmann 1999). It is therefore important to improve the accuracy of weak-lensing mass estimates by minimising systematic errors in particular. This will help us in identifying the assumptions in the X-ray analysis which are responsible for the mass discrepancy as opposed to errors which have their origins in the lensing analysis.

Very deep observations of clusters of galaxies in multiple bands and with sub-arcsecond seeing can considerably improve the reliability of mass estimates from weak lensing; the depth increases the number density of lensed galaxies thereby improving the resolution of the mass reconstruction; multicolour observations allow estimation of photometric redshifts and hence the redshift distribution of background sources; finally, sub-arcsecond seeing makes for a better determination of object shapes and accurate PSF correction. Rarely are all of these stringent requirements satisfied simultaneously in ground based observations. Fortunately, the observations obtained during the Science Verification Programme[1] for the FORS1 (FOcal Reducer/low dispersion Spectrograph; Appenzeller et al. 1998) and the ISAAC (Infrared Spectrometer and Array Camera; Moorwood et al. 1999) instruments mounted on the first VLT unit, UT1/ANTU, at Paranal provide an excellent dataset on the lensing cluster MS 1008–1224.

[1] Details of this dataset are available at the URL `http://www.hq.eso.org/science/ut1sv`

Table 1. Summary of the characteristics of the VLT observations of MS 1008–1224 with FORS1 and ISAAC. Columns 2, 4 and 5 are from from the ESO web site while the seeing ($FWHM$) was obtained from the images themselves.

Filter	Exp. Time (s)	Seeing ($''$)	SB-Lim (mag/arcsec^2)	Scale ($''$/pix)
B	4950	0.72	28.25	0.2
V	5400	0.65	27.90	0.2
R	5400	0.64	27.44	0.2
I	4050	0.55	26.37	0.2
J	2880	0.68	-	0.147
K	3600	0.45	-	0.147

The quality (seeing and depth in 6 bands) of these images are among the best data ever obtained from the ground for weak lensing mass reconstruction of a cluster.

MS 1008–1224 is a galaxy cluster selected from the Einstein Medium Sensitivity Survey (Gioia & Luppino 1994). It is one of the 16 EMSS clusters observed by Le Fèvre et al. (1994) in which they found strong-lensing features. The cluster is at redshift $z = 0.3062$ (Lewis et al. 1999) and is dominated by a cD galaxy. The X-ray luminosity is $L_{\rm X}(0.3\text{–}3.5\,{\rm keV}) = 4.5\times10^{44}\,{\rm erg\,s^{-1}}$ (From Lewis et al. 1999, with $H_0 = 100$ km s^{-1} Mpc^{-1} and $q_0 = 0.1$) and its temperature inferred from ASCA observation is $T_{\rm X} = 7.29$ keV (Mushotzky & Scharf 1997). According to Lewis et al. (1999), the X-ray contours are circular and are centered 15 arcsec to the north of the cD and also show an extension towards the north.

The paper is organized as follows: Sect. 2 details the optical properties of the VLT images. Section 3 deals in some detail with the photometric redshift estimation of galaxies in the field of MS 1008–1224. The mass reconstructions, from weak shear analysis as well as from depletion produced by magnification bias, are presented in Sect. 4. The results are discussed in Sect. 5. Finally, a summary of this study is provided in Sect. 6.

In this paper we have used $H_0 = 100\ h^{-1}$ km s^{-1} Mpc^{-1}, $\Omega_0 = 0.3$, $\Lambda = 0$. This corresponds to a scale of 1 arcmin $= 176\ h^{-1}$ kpc at the redshift of the cluster.

2. Optical properties of the lens MS 1008–1224

The observations were all carried out by the Science Verification Team at ESO. The $6\farcm8 \times 6\farcm8$ field of FORS1 was centred on the cD galaxy in MS 1008–1224 and images were obtained in the B, V, R and I bands. ISAAC was used to obtain $2\farcm5 \times 2\farcm5$ images of the central region of the FORS1 field in the J and K bands. The details of the data processing, from the image acquisition to co-addition and calibration, may be found at the ESO web site (see URL in the previous section) while a summary of the image characteristics are presented in Table 1. The FORS1 field corresponds to a physical size of $1.2\ h^{-1}$ Mpc at $z = 0.31$ and provides a global view of the morphology of MS 1008–1224 and of the field of galaxies around it. Together with

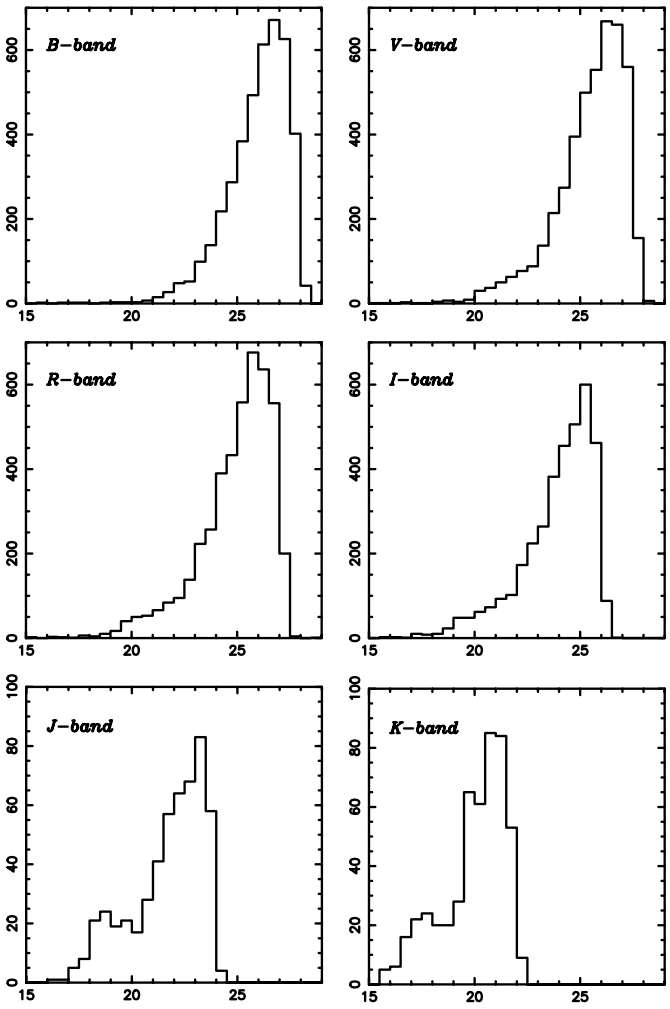

Fig. 1. Histograms of the magnitude distribution of the MS 1008–1224 field: B (top left), V (top right), R (middle left), I (middle right), J (bottom left), K (bottom right).

the X-ray observations of Lewis et al. (1999), these high quality multi-band images are well suited for a detailed analysis of the distribution of mass within the cluster.

Source detection and photometry were performed in a standard manner using SExtractor (version 2.1.0; Bertin & Arnoults 1996). The magnitude distributions of galaxies are shown in Fig. 1. The photometric accuracy is better than 0.1 mag up to $B \sim 26.5$, $V \sim 26.5$, $R \sim 25.8$, $I \sim 24.5$, $J \sim 22$ and $K \sim 20$. The stars in the field were identified by their location on the magnitude – half-light radius plot (Fahlman et al. 1994). This method easily and unambiguously separates stellar objects from extended ones up to $I \sim 22$ or $R \sim 23$ and provides enough stars to determine the PSF variation across the FORS1 field. We note here that the expected fraction of stars at fainter magnitudes is negligible (Griffiths et al. 1994; Conti et al. 1999) and hence is not a matter of significant concern for the weak-lensing analysis.

3. Redshift distribution of galaxies in the MS 1008-1224 field

3.1. Photometric redshift estimation

Photometric redshifts (hereafter $z_{\rm phot}$) were computed using the standard fitting procedure *hyperz* (Bolzonella et al. 2000) which compares the observed spectral energy distribution (SED) of a given galaxy, obtained from photometry, to a set of template spectra. Redshifts are then computed using a standard χ^2 minimization. *hyperz* explores the parameter space defined by the age and metallicity of the stellar population, the IMF, the reddening law and the reddening value. When tested against the HDF spectroscopic sample $z_{\rm phot}$ errors from *hyperz* were found to be $\Delta z \sim 0.05$ at $z \leq 1$, and $\Delta z \sim 0.1(1+z)$ for more distant galaxies (see Bolzonella et al. 2000 for more details).

For this work, we used a set of 8 template families from the new Bruzual & Charlot evolutionary code (GISSEL98; Bruzual & Charlot 1993) with a Miller & Scalo IMF. The families spanned a wide range of ages for the stellar population and included: a single burst (coeval stellar population), a constant star-forming rate, and six μ-models (exponentially decaying SFR) designed to match the sequence of colours from E-S0 to Sd galaxies (255 spectra in all). The reddening law was taken from Calzetti et al. (2000) with values of A_V between 0 and 1.2 mag, the upper value being twice the mean $E(B-V)$ reported by Steidel et al. (1999) for galaxies up to $z \sim 4$. The Lyman forest blanketing was modelled according to Madau (1995). *hyperz* computes error bars corresponding to 69, 90 and 99 per cent confidence levels computed by means of the $\Delta\chi^2$ increment for a single parameter (Avni 1976). We only considered a $z_{\rm phot}$ estimate when the best fit template had $\chi^2 < 1$. It may be noted that errors in the photometry of the MS 1008–1224 field were more significant than uncertainties in the template spectra used.

The accuracy and robustness of $z_{\rm phot}$ were investigated using simulated catalogues of galaxies with realitics SEDs. The error budget and $z_{\rm phot}$ accuracy were then analysed as a function of the ESO-*BVRIJK* filter set, the photometric errors and the redshift range of the simulated galaxies.

First, catalogues were produced for the two sets of filters, *BVRI* (FORS1 images alone) and *BVRIJK* (field common to FORS1 and ISAAC images), assuming a uniform redshift distribution and a Gaussian photometric error distribution of fixed sigma (0.1 mag), uncorrelated between the different filters. These were used to determine (i) $z_{\rm phot}$ errors, (ii) the fraction of sources for which *hyperz* returned either no solution ($\chi^2 > 1$) or multiple solutions and (iii) the fraction of sources with spurious values (i.e., errors much larger than the normal dispersion at that redshift). The uniform distribution of simulated galaxies across the redshift range provided a sufficient number of objects for a robust estimation of the errors at all redshifts.

We then performed a second set of simulations using a pure luminosity evolution (PLE) model. The redshift distribution and the photometric errors (a function of

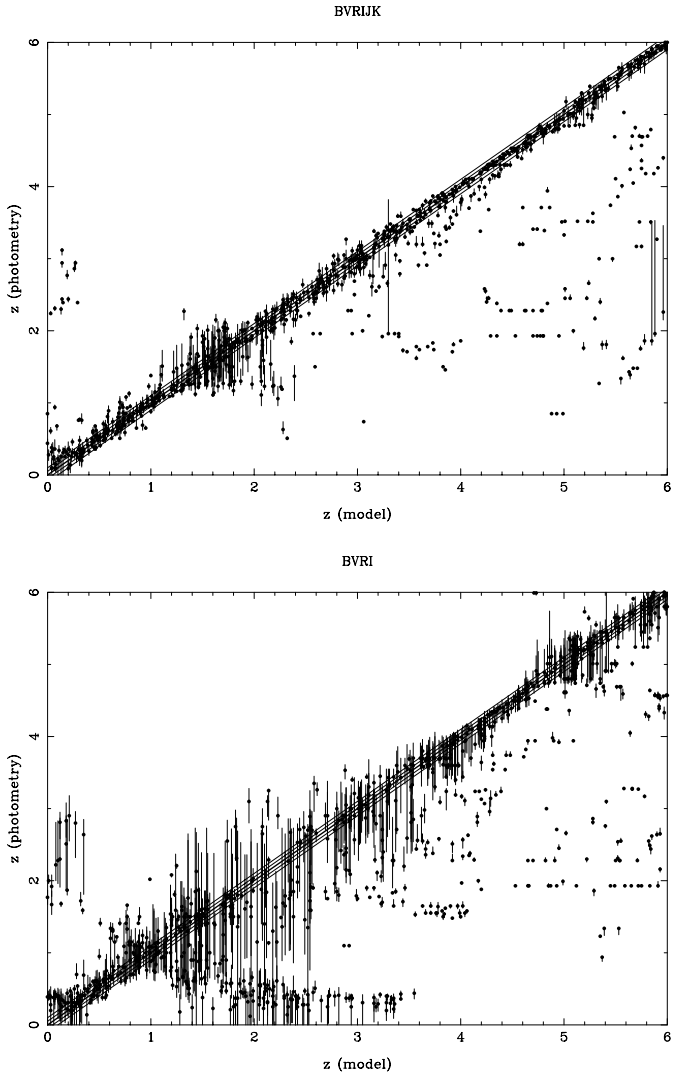

Fig. 2. Photometric versus model redshift for a simulated catalogue of galaxies uniformly distributed in redshift and a 10% photometric error. Error bars of $\pm 1\sigma$ are shown for each object. The 5 diagonal lines plotted are $z_{\rm phot} = z(\rm model)$, $z_{\rm phot} = z(\rm model) \pm 0.05$ and $z_{\rm phot} = z(\rm model) \pm 0.1$. Top panel: $z_{\rm phot}$ computed using *BVRIJK* photometry. Bottom panel: $z_{\rm phot}$ computed using *BVRI* photometry.

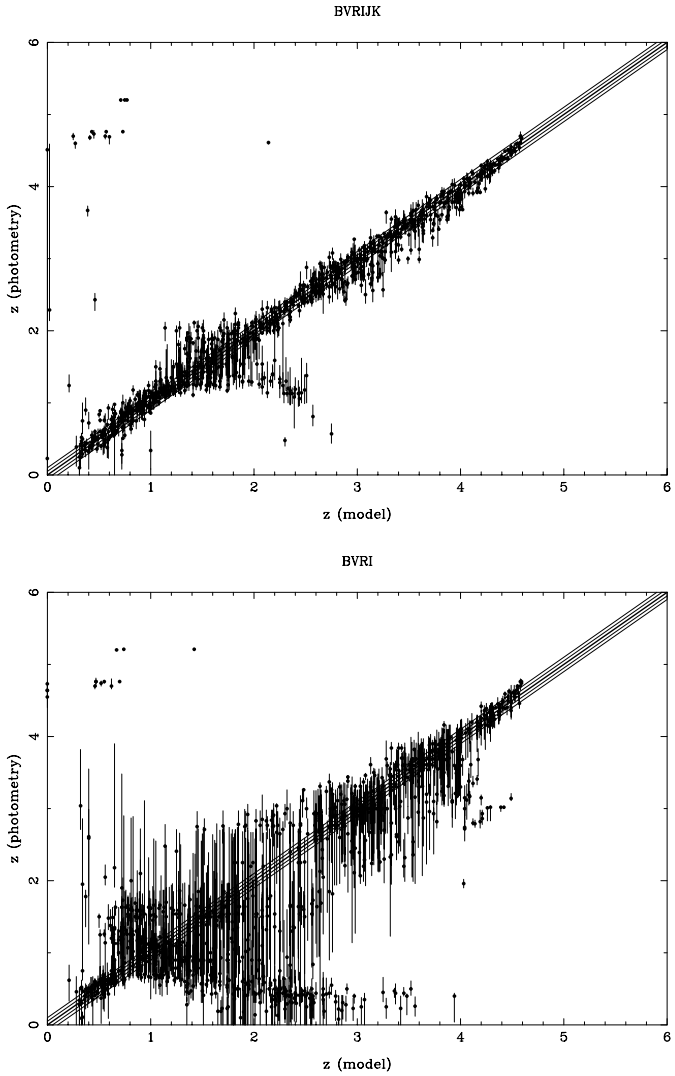

Fig. 3. Photometric versus model redshift for a simulated catalogue of galaxies simulated to match the data in hand, with a PLE number counts model and photometric errors scaling with magnitude. Error bars of $\pm 1\sigma$ are shown for each object. The 5 diagonal lines plotted are $z_{\rm phot} = z(\rm model)$, $z_{\rm phot} = z(\rm model) \pm 0.05$ and $z_{\rm phot} = z(\rm model) \pm 0.1$. Top panel: $z_{\rm phot}$ computed using *BVRIJK* photometry. Bottom panel: $z_{\rm phot}$ computed using *BVRI* photometry.

magnitude and filter) in this second simulation were tailored to mimic the VLT observations of the MS 1008–1224 field in a more realistic manner. In particular, we focussed on (simulated) galaxies in the range $22.5 \leq R \leq 26.5$ (shear analysis sample) and $22.5 \leq I \leq 25.5$ (depletion analysis sample). Galaxies were assigned magnitudes and colours randomly according to the PLE model of Pozzetti et al. (1998) which had been designed to reproduce the deep B counts (Williams et al. 1996).

The results from the simulations are shown in Fig. 2 (uniform redshift distribution) and Fig. 3 (PLE distribution). It is clear from these plots that most galaxies with *BVRIJK* magnitudes will have fairly well determined $z_{\rm phot}$. Typical uncertainties scale as $\Delta z_{1\sigma} \sim 0.1(1+z)$, and the fraction of objects with no solution or spurious values is only a few per cent. Therefore we are confident that the redshift distribution of galaxies on the ISAAC field has been well determined. In contrast, the situation is less satifying when using only *BVRI* in the redshift range $0.8 \leq z \leq 2.5$. This is due to the lack of strong spectral features in the wavelengths covered by these filters. The main problem in this case is the translocation of some fraction of $z \geq 1$ objects into lower redshift bins.

The redshift ($z_{\rm phot}$) distribution of sources in the ISAAC field is shown in Fig. 4. This distribution comprises galaxies for which *hyperz* returned a unique $z_{\rm phot}$ value with a good model fit ($\chi^2 < 1$). To satisfy this criterion we excluded blended sources from the analysis.

The cluster of galaxies comprising MS 1008–1224 is an "in–situ" control sample for checking the accuracy of our $z_{\rm phot}$ estimation. Indeed, the cluster shows up as a

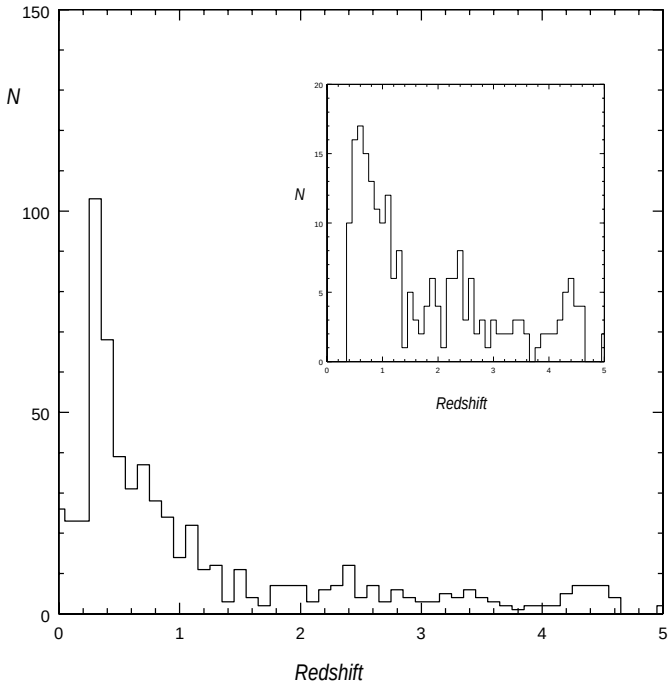

Fig. 4. Photometric redshift distribution of galaxies inside the ISAAC field obtained from *BVRIJK* data. The peak corresponds to the cluster MS 1088–1224. Only those galaxies which fit the *hyperz* models with $\chi^2 < 1$ are plotted here (see Sect. 3). The inset histogram represents galaxies with $22.5 \leq I \leq 25.5$ and $z_{\rm phot} \geq 0.4$ (i.e. well behind the cluster).

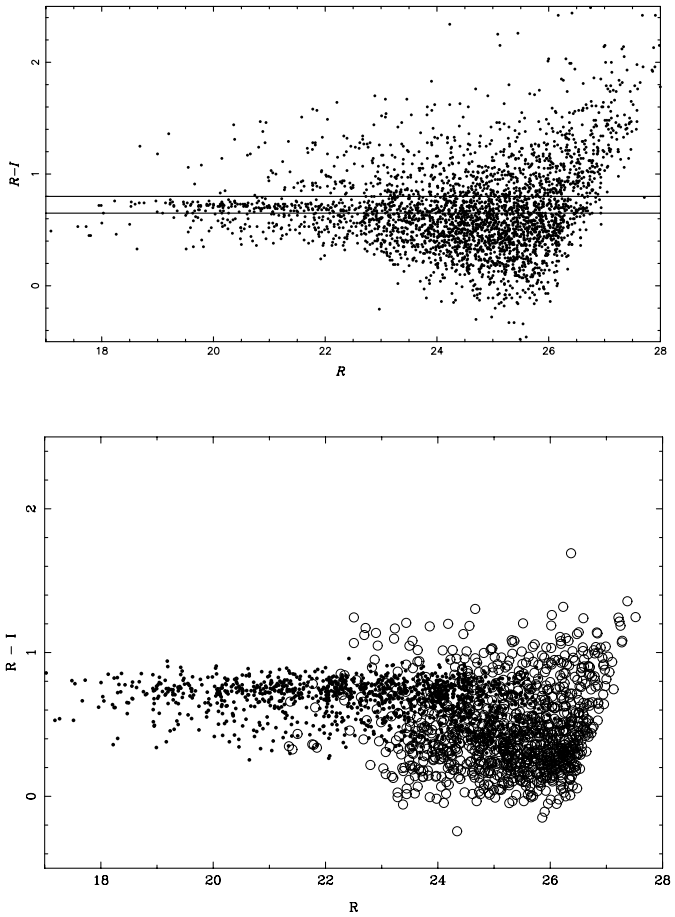

Fig. 5. Top: a Colour-Magnitude ($R-I$ vs. R) plot for the field of MS 1008–1224. The cluster sequence formed by galaxies belonging to MS 1008–1224 is clearly visible as a horizontal strip at $R-I = 0.69 \pm 0.15$. Bottom: colour-magnitude plot for a simulated cluster field. Cluster and field galaxies are displayed as black dots and open circles respectively.

prominent spike in the $z_{\rm phot}$ distribution (Fig. 4) between $z = 0.25$ and 0.4 ($z_{\rm mean} \sim 0.34$) which confirms both the efficacy of the method as well as our error estimates from simulations. An additional, and unexpected, check was provided by the discovery of a background cluster at $z_{\rm phot} \sim 0.9$. That a number of galaxies were clustered in redshift space as well as on the sky suggested that their $z_{\rm phot}$ value was reasonably accurate.

3.2. Distribution of cluster galaxies

We also simulated cluster fields at $z = 0.31$ as targets for the *hyperz* program. The clusters were generated with galaxies distributed according to a King model with central line-of-sight velocity dispersion of 1000 km s^{-1}, a core radius of 500 kpc and a Schecter luminosity distribution in the range $-14 \leq M_B \leq -22$. The mixture included 70 per cent ellipticals and S0 galaxies, 28 per cent spirals and 2 per cent star-forming galaxies. The other parameters (IMF, SFR, models etc.) were as described before. The photometric accuracy (as a function of magnitude) and limiting magnitudes were chosen to match the observed values for MS 1008–1224. The apparent magnitudes in all filters were computed through GISSEL98. This simulated cluster catalogue was added to a PLE field catalogue to simulate the observed catalogue.

Figure 5 shows the cluster sequence on the observed Colour-Magnitude plot $R-I$ vs. R. It is almost horizontal for these filters. The same Colour-Magnitude diagram is also plotted for a realization of the simulated cluster described above and is very similar to the actual data.

Simulations indicated that the error in $z_{\rm phot}$ for cluster members was $\sim$0.04 (1σ) which is similar to the width of the peak obtained for real data (Fig. 4). It may be noted that this accuracy is much better than $\Delta z_{1\sigma} \sim 0.1(1+z)$ because of the presence of appropriately located spectral features which make identification of red cluster galaxies particularly easy in this redshift range. It is also clear that the cluster redshift distribution is skewed, the lower redshift side of the peak being considerably steeper than its counterpart. So we defined the foreground galaxy sample as those at $z_{\rm phot} < 0.25$ and the background sample (for lensing analysis) as those at (conservatively) $z_{\rm phot} > 0.4$. *hyperz* detected 75 per cent of the simulated cluster galaxies in the range $0.25 \leq z_{\rm model} \leq 0.35$ with *BVRIJK*.

One of the problems with using the *BVRI* photometry for $z_{\rm phot}$ is the contamination of lower redshift bins by interlopers from $z > 1$ and this could be higher than 1 in 3 sources. On the contrary, the simulated Colour-Magnitude diagram in Fig. 4 indicated that the cluster luminosity is dominated (80–90 per cent) by

emission from red ellipticals on the cluster sequence. Carlberg et al. (1996) estimated that the red galaxies on the cluster sequence underestimate the cluster luminosity by about 15 per cent, similar to what we see in our simulated data. So we used galaxies from the entire FORS1 field on the cluster sequence of the Colour-Magnitude diagram ($R-I = 0.69\pm0.15, 17.5 < R < 24.0$) for calculating the luminosity distribution and applied the 15% correction determined above.

The number and luminosity density distributions of cluster galaxies are shown in Fig. 6. The distributions were obtained by computing the local galaxy number density at each galaxy position followed by a smoothing of the resulting density field by a Gaussian of 50 arcsec *FWHM*. There was no significant change when the cluster magnitude limit was extended to $R = 27$. The galaxy numbers and luminosity show a strong concentration around the cD and a northward extension. One can discern four prominent peaks in both distributions at ($x_{\rm arcsec}$, $y_{\rm arcsec}$) $\equiv$ (220, 220), corresponding to the location of the cD galaxy, (200, 280), (240, 380), (260, 300) and (360, 160). The coherent substructures indicated by the coincidence of light and number peaks suggests that MS 1008–1224 is not yet dynamically relaxed.

3.3. The redshift distribution and lensing analysis

We used photometric redshifts to calculate the average lensing distance modulus to convert the gravitational convergence (shear analysis) into a mass estimate. Thus missing the $z \geq 1$ objects from *BVRI* photometry would have resulted in a considerable error in the absolute mass estimate. Therefore we assumed that the redshift distribution in the ISAAC field (i.e. those sources which had *BVRIJK* magnitudes) was representative of the whole FORS1 field.

The redshift of background sources affects the mass estimate only through the angular scale distance which has a weak redshift dependence at $z > 0.5$ in most cosmologies. So $\delta z_{\rm phot} = 0.1-0.2$ is not of much concern, especially when compared to other sources of error discussed in the section on shear analysis. We also used the $z_{\rm phot}$ distribution to determine the foreground source contamination of the lensing sample which would have diluted the lensing signal and corrected for the same.

4. Gravitational lensing analysis in MS 1008–1224

4.1. Mass reconstruction from weak shear

The weak distortion of background sources produced by gravitational lenses can be used to construct the projected mass distribution of the lens (see Tyson et al. 1990; Mellier 1999; Bartelmann & Schneider 2000). The excellent quality of the FORS1 data-set, especially the depth and the seeing, enabled us to accurately correct for many of the non-gravitational distortions of the image (PSF shear/smear) and also explore in some detail issues like fidelity of reconstructed mass features. To do this two teams, using different source selection criteria and different mass reconstruction schemes, independently produced maps of the mass distribution in MS 1008–1224.

4.1.1. 2-dim mass reconstruction algorithms

Method 1

The IMCAT weak-lensing analysis package has been made publicly available at the URL `http://www.ifa.hawaii.edu/~kaiser` by Kaiser and his collaborators (Kaiser et al. 1995; Luppino & Kaiser 1997). The specific version used was the one modified and kindly made available to us by Hoekstra (see Hoekstra et al. 1998). A description of the analysis including measurement of the galaxy polarization, correction for smearing by and anisotropy of the PSF and the shear polarizability of galaxies and the expression for the final shear estimate have already been given by Hoekstra et al. (1998) and references therein and will not be repeated here.

The PSF anisotropy varied across the image and was about 0.015 (shape polarisation). The variation across the image was determined and corrected (separately in each band) using 50–60 stars scattered all over the CCD. The correction resulted in a mean residual polarisation of 0.0002 (rms = 0.004) for these PSF stars.

The maximum probability algorithm of Squires & Kaiser (1996), with $K = 20$ (number of wave modes) and $\alpha = 0.05$ (the regularisation parameter), was used to reconstruct the mass distribution from the shear field. Our analysis differs from that of Hoekstra et al. only in the weighting of the data at the final stage (described next).

Error weighting: The contribution of gravitational shear to the observed ellipticity of a background source is only a small fraction of its intrinsic ellipticity and so one has to average the shapes of many (10–20) sources in the neighbourhood to estimate the gravitational shear at that location. Further, the individual values *have* to be appropriately weighted to obtain meaningful results. Following Hoekstra et al., we estimated the average value of the shear at a location $\langle\gamma\rangle = \Sigma(W_i\gamma_i)/\Sigma W_i$, where γ_i is the shear of individual galaxies and $W_i = G_i/(\delta\gamma_i)^2$ is the weight comprising the error on the individual shear ($\delta\gamma_i$) and a Gaussian factor G_i depending on the distance of the i-th galaxy from the location at which the average shear was being calculated. The typical value of $\delta\gamma_i$ was about 0.45, including the scatter due to intrinsic polarisation ($\sim$0.25) added in quadrature to measurement error (photon noise). Foreground galaxies were used to determine the intrinsic polarisation distribution. The smoothed shear field was determined for both the components of shear and these were used by the mass reconstruction programme along with appropriate co-efficients to generate the mass map.

While this method works quite well it has the disadvantage that the error weighting and the Gaussian smoothing are coupled to each other. Decreasing the

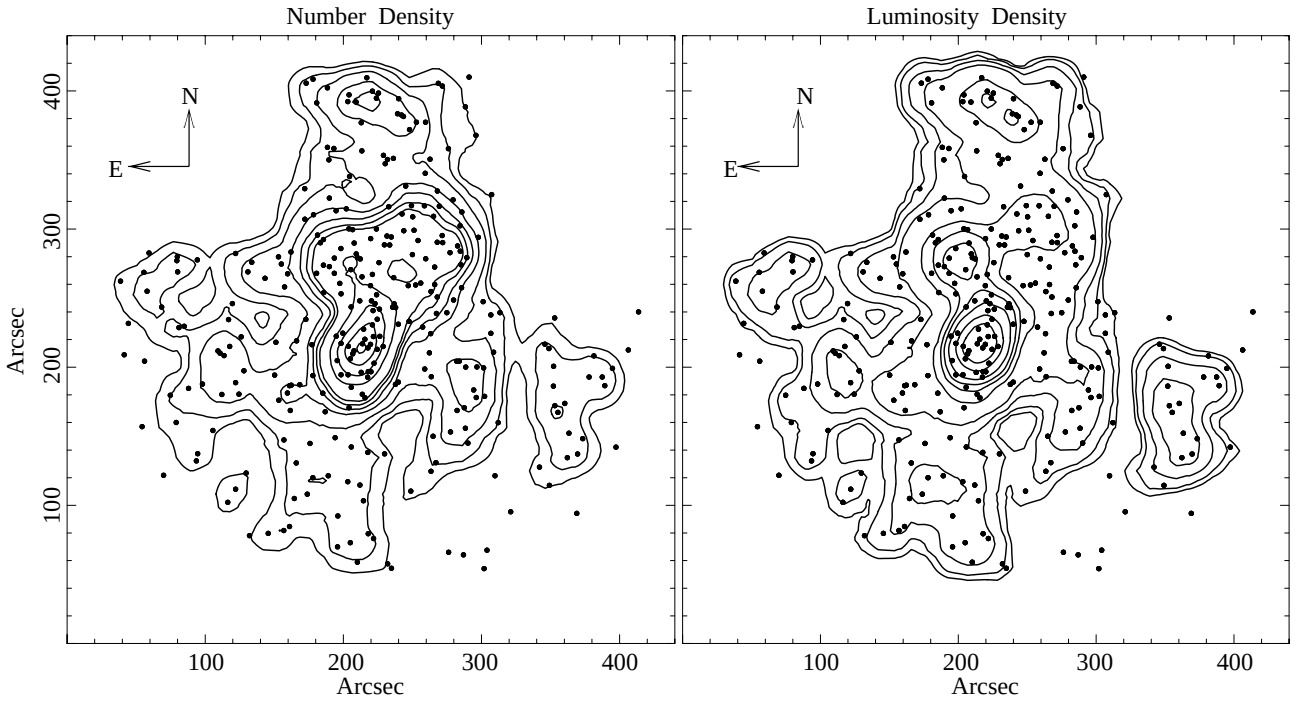

Fig. 6. Galaxy number and R-band luminosity density distribution in the galaxy cluster MS 1008–1224. The densities were computed from galaxies on the cluster sequence on the Colour-Magnitude plot (see Fig. 5 and the text) and smoothed with a $50''$ Gaussian. The average galaxy number density is 5.9 gal arcmin^{-1}. The number density contours plotted (left) are 12.0, 24.0, 36.0, 72.0, 144.0, 215.0, 280.0, 360.0, 720.0, 1080.0, 1440.0, and 1800.0 gal arcmin^{-2}. So, the density contrast reaches 305 in the cluster center with respect to the average value. The average luminosity over the field is $0.0021 \times 10^{13}\ h^{-1}\ L_{\odot}$ arcmin^{-2}. The luminosity density contours plotted (right) are 0.0015, 0.003, 0.005, 0.01, 0.02, 0.07, 0.12, 0.2, 0.3, 0.5 and $0.7 \times 10^{13}\ h^{-2}\ L_{\odot}$ arcmin^{-2}. So the luminosity contrast at the cluster center is 330.

Gaussian smoothing scale (to investigate finer structure in the mass map) reduces the effectiveness of the all important error weighting; in the limiting case when the Gaussian smoothing scale includes just one background source (on the average) there is no error weighting at all. Since lensing inversion is a highly non-linear process and the individual shear values were dominated by the errors on them, this resulted in the final reconstructed mass distributions being considerably dependent on the smoothing scale used. Often we could not discern any signal at all in the mass map when small smoothing scales were used.

To remedy this, apart from $\langle\gamma\rangle$ we also calculated the error on it, $\delta\langle\gamma\rangle = \Sigma(G_i/\delta\gamma_i)^2/[\Sigma(G_i/(\delta\gamma_i)^2)]^2$ and used this to weight the shear values in the mass reconstruction algorithm. This removed the dependence of error weighting on the smoothing scale and made it possible to make mass maps with very small smoothing scales to (i) confirm that the lower resolution mass maps could be obtained by a post-reconstruction smoothing of the higher resolution map which indicated that our error-weighting and hence error estimates were correct, (ii) check the stability of the individual features seen in the mass reconstruction and (ii) investigate the mass distribution in better detail.

Source selection: The source detection was done in the R-band using both IMCAT and SExtractor. Only those background (to the cluster) sources which were detected by IMCAT with a significance >7 and were also detected by SExtractor were used for the lensing analysis. Sources with neighbors closer than 5 pixels (1 arcsec) were eliminated to reduce the error in the shape estimation. With a series of subsamples spanning a narrow range of $\delta R = 0.5$ mag, we detected using Aperture Mass densitometry (described later) a lensing signal for sources in the range $22.5 < R < 26.5$. This constituted our master list of 2550 sources for the mass reconstruction analysis. The sources from this master list which were detected in the other 3 bands ($B \equiv 2080$, $V \equiv 2423$ and $I \equiv 2417$ sources) constituted the lensing analysis sample for those bands.

Quality of the mass reconstruction: One of the advantages of using an FFT algorithm is that an output length scale is a natural feature and may be easily specified using certain parameters. This matching of the output resolution (of the mass-map) with the input shear field smoothing scale and data quality (for e.g., more wavemodes for better quality shear data and for higher resolution images) allowed us to make reconstuctions with different output resolutions to check the fidelity of mass features.

However, it has disadvantages as well. Any hole in the shear field (caused by a bright star, for example) is filled in with zeros by the algorithm leading to strong ripples and negative peaks in the reconstucted image. As a result one sometimes finds egregious artifacts which are

5–10 times larger than the noise. In general, the noise calculated over small regions (i.e. the "true" noise which avoids large scale correlated fluctuations) is 3–5 times smaller than an rms calculated over a large area including ripples and all. However, this latter quantity is perhaps more appropriate for determining the significance of the features in the mass maps and is the value listed in the figure captions. It must be noted that this is not the rms of a Gaussian random distribution and hence the usual rules of thumb and relationships of Gaussian distributions (e.g. $>3\sigma$ is significant) may not always be appropriate. We discuss below some of the ways, some heuristic and others more solid, in which we can deduce the reliability of the features seen in the mass reconstruction:
(i) The *Curl*-map: the shear field is a function of the gradient of the gravitational potential and so a mass map made from the *curl* of the shear field (effectively replacing γ_1 by $-\gamma_2$ and γ_2 by γ_1) must produce a structure-less noise map (Kaiser 1995) in the absence of systematic errors in the shear field. Thus, such a *Curl*-map may be expected to indicate the location and intensity of artifacts. Further, since the *Curl*-map is essentially free of source regions most of its pixels can be used to get a good estimate of the "large-scale" rms discussed earlier.
(ii) Bootstrap techniques.
(iii) Compare mass maps made with different smoothing scales: features which vary from one scale to another in an inconsistent manner are likely to be artifacts.
(iv) Compare mass maps made with data from different bands: the shape of each lensed galaxy is approximately (but not exactly) the same in every band though the final shape should be different due to different PSFs and photon noise, especially for faint sources. It is necessary that a feature, in order to be considered real, should be of similar shape and intensity (within errors) in all the bands. Since the noise is so much stronger than the shear signal reproducing the same features in all the bands is an indication that PSF corrections and noise weighting were handled appropriately. Of course, this check is not sufficient to prove that the features are real since intrinsic ellipticities and locations of the background galaxies are similar/same in all the bands (see next point).
(v) Random shuffling of the Shear: the shear is sampled only at the positions of the background sources. Therefore, this multiplicative sampling function leaves its own convolved footprint on the mass map. However one can get a qualitative idea of the effect by keeping the positions fixed and randomly shuffling the observed shear values among them. Obviously this should again result in a structure-less noise map if there were no systematics introduced by the sampling function and the FFT.
(vi) An inspection of the location and significance (in terms of rms) of the negative peaks on the mass map itself.

Method 2

This method also used the raw IMCAT software from Kaiser's home page (see previous method) with some minor modifications for estimating the shear field. The mass reconstruction was done using the maximum likelihood estimator developed by Bartelmann et al. (1996) with the finite difference scheme described in Appendix B of Van Waerbeke et al. (1999). The reconstruction was not regularised and hence the resulting mass maps were noisier than those obtained from Method 1. However, as pointed out Van Waerbeke et al. (1999) and Van Waerbeke (2000) the advantage of method 2 is that the noise can be described analytically in the weak lensing approximation. When galaxy ellipticities are smoothed with a Gaussian window

$$W(\boldsymbol{\theta}) = \frac{1}{\pi\theta_{\rm c}^2}\exp\left(-\frac{|\boldsymbol{\theta}|^2}{\theta_{\rm c}^2}\right). \quad (1)$$

The noise in the reconstructed mass map is a 2-D Gaussian random field fully specified by the noise correlation function (Van Waerbeke 2000):

$$\langle N(\boldsymbol{\theta})N(\boldsymbol{\theta}')\rangle = \frac{\sigma_\epsilon^2}{2}\frac{1}{2\pi\theta_{\rm c}^2 n_{\rm g}}\exp\left(-\frac{|\boldsymbol{\theta}-\boldsymbol{\theta}'|^2}{\theta_{\rm c}^2}\right). \quad (2)$$

We used this property to simulate shear fields (including the appropriate noise) to derive the positional stability of mass features and hence the significance of the offset between the mass centroid and the cD galaxy.

4.1.2. Distribution of the dark matter in MS 1008–1224

The mass reconstructions from B, V, R and I data using the first method are shown in Fig. 7 (30 arcsec smoothing scale) and Fig. 8 (15 arcsec smoothing scale).

Features in the mass maps: The lower resolution reconstructions (Fig. 7) are very similar in shape as well as magnitude of the peak (±5 per cent variation). The main features are a central mass condensation which seems to be elongated in the north-south direction, a fainter extension towards the north and a ridge leading off towards the north-east from the main component. The prominent cross at (222, 222) marks the location of the cD galaxy.

The higher resolution image (Fig. 8) clearly resolves the principal mass component into 2 peaks separated along (mostly) the north-south direction. Once again, it may be noted that the structures are similar in all the bands. We also note that the northern peak appears to be marginally higher than the southern one in all images. This montage (Fig. 8) also includes an average of the mass maps in the 4 bands (bottom-left). The concentric circles denote the annuli within which the mass was estimated to determine the radial profile. They are centred on the centroid of the mass distribution (the black dot) determined from the average of the lower resolution maps (Fig. 7). It must be noted that averaging the mass distribution from all the 4 bands does reduce the amplitude of spurious ripples relative to the more stable mass peaks but not by a

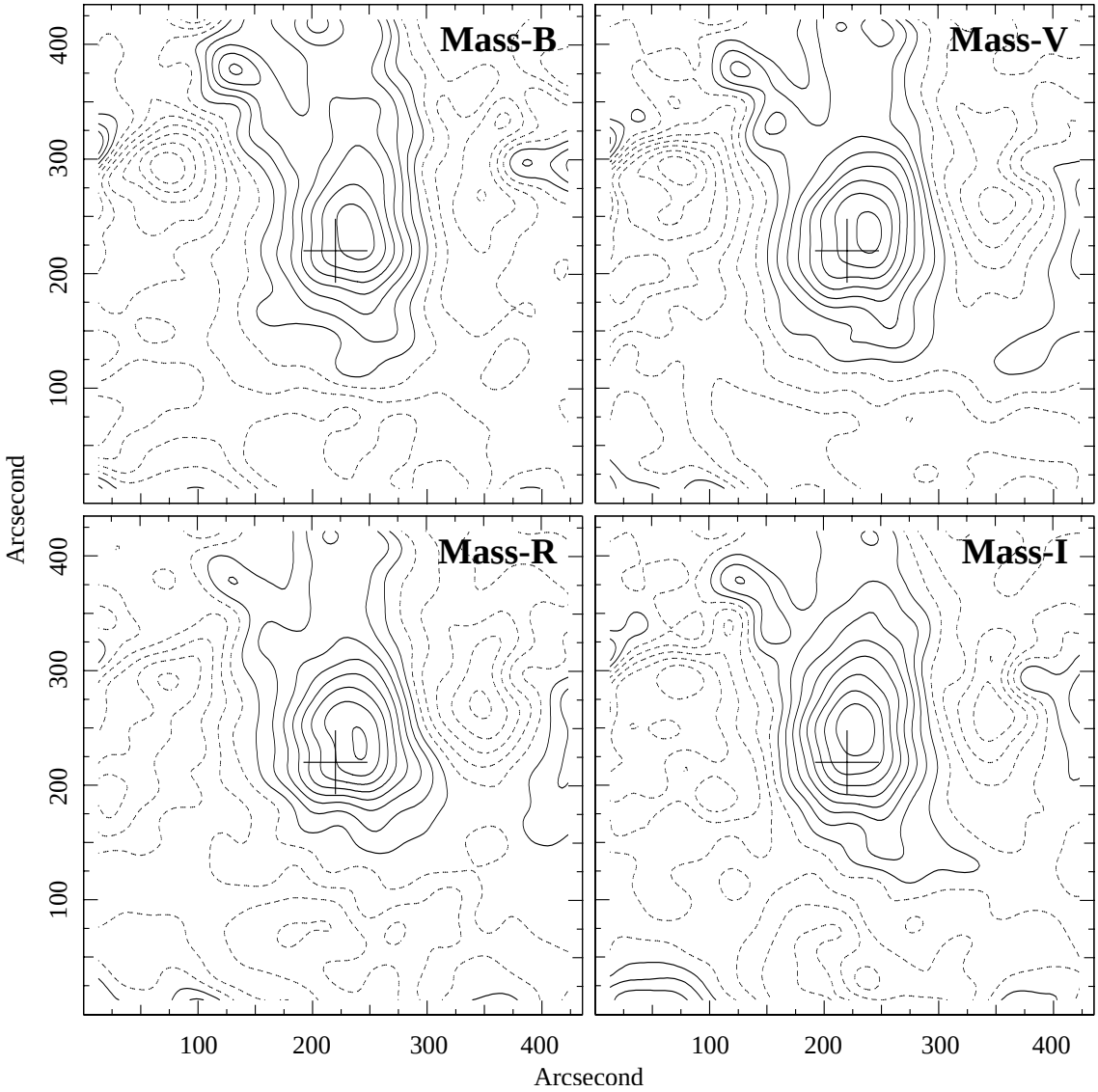

Fig. 7. Mass reconstruction of MS 1008–1224 from B, V, R and I images using the algorithm of Squires & Kaiser (1996) – Method 1 in the text – and a Gaussian smoothing of 30 arcsec. The iso-convergence contour interval is $\kappa = 0.025$. Broken contours represent negative values and the first solid contour delineates $\kappa = 0$. The rms is about 0.025. The cross at (222, 222) marks the location of the cD galaxy. North is to the top and east is to the left.

factor of 2; for one, the noise is not Gaussian and for another, averaging the shear field with data from different bands reduces the photon noise but not the noise due to intrinsic galaxy ellipticity.

Also shown on the same plot is an average of the *Curl*-maps made in each of the 4 bands (bottom-right). There were two very bright stars in the MS 1008–1224 field which were masked on the FORS1 images. The thick curved lines delineate the extent of these masks from where no shear data was available. These holes in the shear field led to strong spurious peaks and ripples in the mass map.

Interpreting the mass features: The two mass components at the centre are the most significant features in all the maps. Their stability across the different bands and smoothing scales as well as their high level of significance is a strong indicator that they are real features.

An inspection of the mass maps in Figs. 7 and 8 clearly shows that the strongest negative peak in each is in the region of the masks. Further, the north-eastern ridge mentioned earlier is along the boundary of one of the masks, its intensity varies from band to band (in contrast to the 2 principal mass components) and is very prominent in the *Curl*-map. So we concluded that it was a spurious feature spawned by the FFT and the masks. It was heartening to note that the strong spurious peaks generated by the masks were confined to their immediate vicinity and that much of the *Curl*-map, especially the lower half, mimics random noise with no strong features.

It is more difficult to determine if the faint but extensive signal leading to the north has a basis in reality.

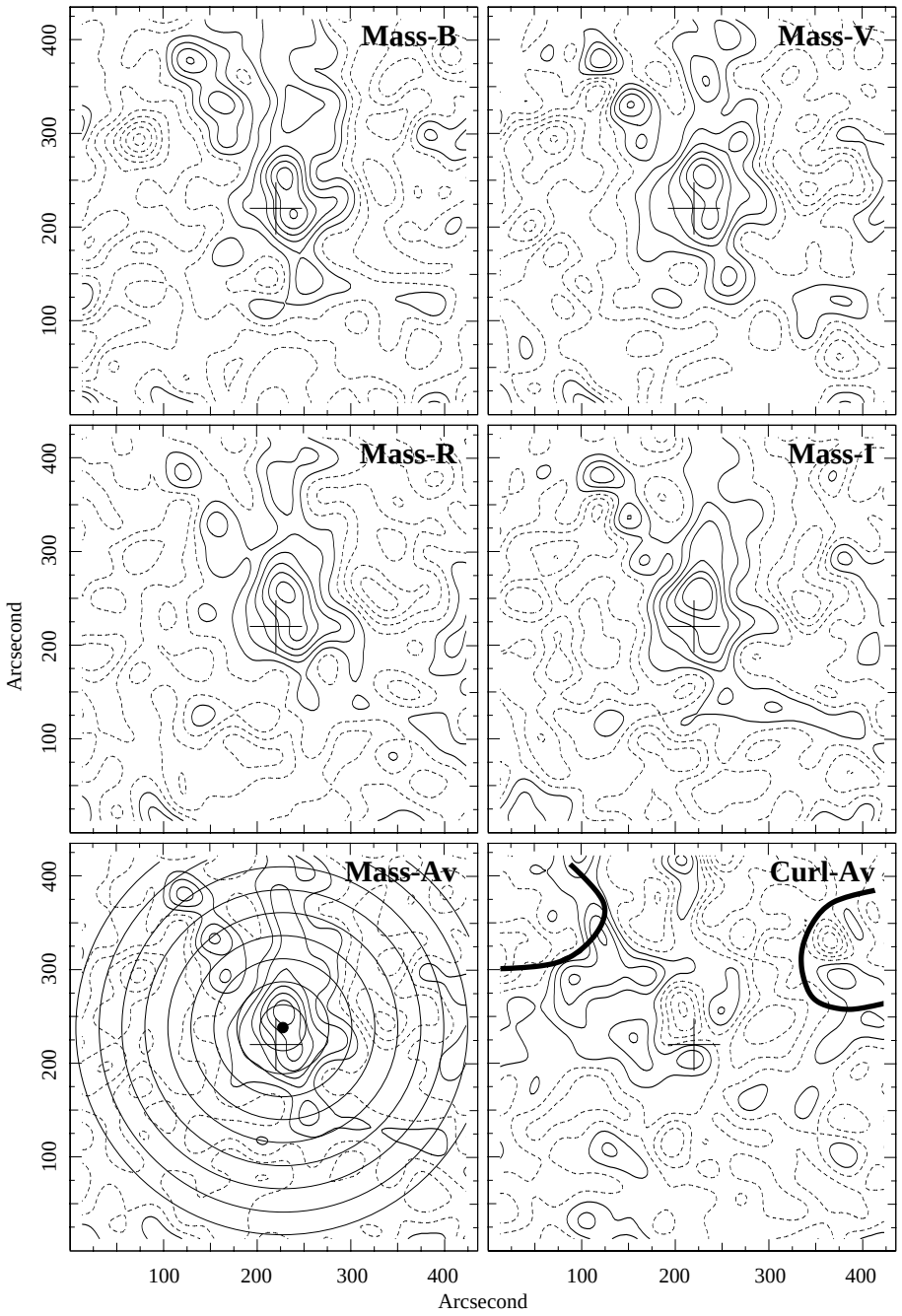

Fig. 8. Mass reconstruction of MS 1008–1224 from B, V, R and I images using the algorithm of Squires & Kaiser (1996) – Method 1 in the text – and a Gaussian smoothing of 15 arcsec. The bottom-left plot is the average of the 4 upper plots while the bottom-right is the average of the *Curl*-map in each band. The iso-convergence contour interval is $\kappa = 0.05$. Broken contours represent negative values and the first solid contour delineates $\kappa = 0$. The rms is about 0.05. The cross at (222, 222) marks the location of the cD galaxy. The concentric circles in the bottom-left plot, spaced $0\farcm4$ apart, indicate the annuli used to determine the radial shear and mass profiles (Figs. 12 and 13); they are centred on the centroid of the mass distribution determined from the low resolution maps (Fig. 7). The two thick curved lines on the bottom-right plot trace the boundaries of the masks on the FORS1 images (to hide two very bright stars). North is to the top and east is to the left.

Given its faintness its considerable fluctuation from one map to another is only to be expected. But to a greater or lesser extent it is present in every single plot including others (not shown in this paper) obtained from different combinations of smoothing scale and wave-modes. So, we tentatively suggest that it is real but we shall not attempt to mine it for any further information. We only note that the cluster number and luminosity density distributions (Fig. 6) also show secondary peaks towards the north.

Another point that we shall discuss in more detail a little later is the offset between the cD galaxy and the centroid of the mass distribution.

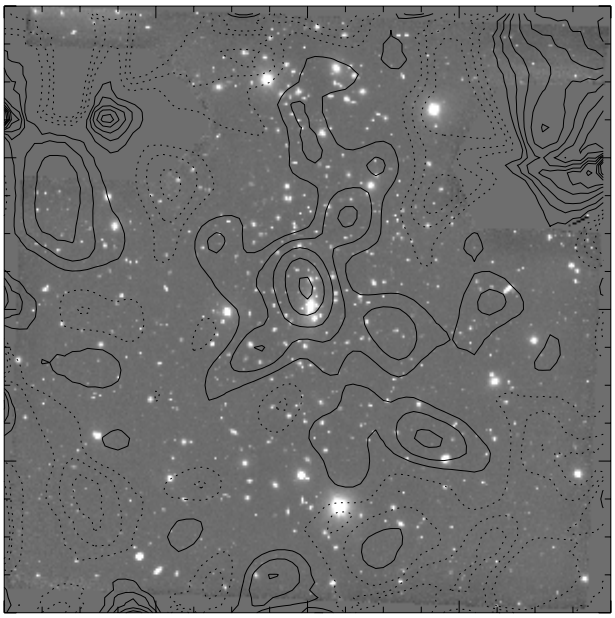

Fig. 9. Mass distribution of MS 1008–1224 using Method 2 and a Gaussian smoothing of 20 arcsec. It is superposed on the full R-band image obtained with the FORS1 on the VLT (440 arcsec on each side with north to the top and east to the left). The cD is the bright object located just below the central mass peak. The iso-convergence (κ) contour values are $\ldots -3\sigma, -2\sigma, -1\sigma, 1\sigma, 2\sigma, 3\sigma, \ldots$ ($1\sigma = 0.05$).

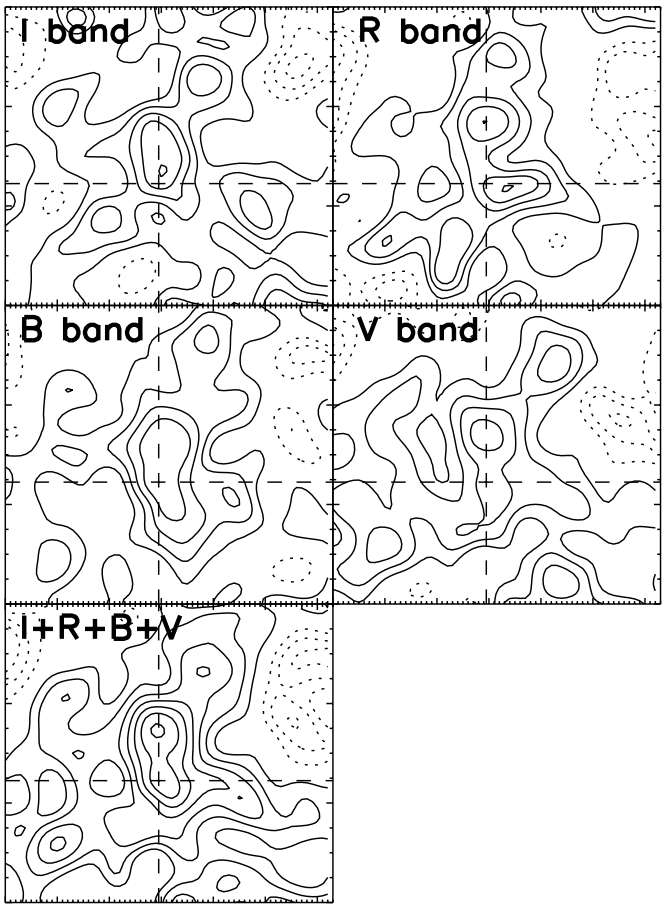

Fig. 10. High resolution mass reconstruction of MS 1008–1224 using Method 2 and a smoothing scale of 15 arcsec. The final plot was obtained by averaging the mass reconstructions in the 4 different bands. This averaging reduces the noise due to measurement error by a factor of 2 (but not that due to intrinsic ellipticity). The iso-convergence (κ) contour values are $\ldots -3\sigma, -2\sigma, -1\sigma, 1\sigma, 2\sigma, 3\sigma, \ldots$ ($1\sigma = 0.07$). Each plot is 215 arcsec on a side with north to the top and east to the left. The crosswires mark the position of the cD galaxy. These maps are to be compared with the ones in Fig. 8 (method 1).

Comparison with method 2: The mass reconstructions obtained using method 2 are shown in Figs. 9 and 10 (20 and 15 arcsec smoothing scales, respectively). Clearly, the plot in Fig. 9, constructed using an intermediate smoothing scale, shows a resolution in between those seen in Figs. 7 and 8. The plots in Figs. 8 and 10 used the same resolution (but different algorithms) and indeed are very similar.

We compared the two methods quantitatively by carrying out a Pearson's r-test (Press et al. 1992) on the high resolution mass reconstructions (the Fig. 8 "Mass-av" image of method 1 and Fig. 10 "$I + R + B + V$" image of method 2). We obtained an r-coefficient of 0.837 for on-signal pixels and $r = 0.298$ for off-signal pixels. The smallest rectangle enclosing the 3σ κ contours of both images defined the on-signal region while the bottom quarter of the image was used for the off-signal region since this was the only clean area lacking the spurious features generated by the large masks in the upper half of the images (see Fig. 8 bottom-right plot). The on-signal correlation is very high and as expected much higher than the off-signal correlation. However the off-signal is still correlated because many galaxies are common in both methods (locations and shapes are the same), which will lead to correlated structures at the noise level throughout the map. Joffre et al. (2000) also measured a similar high correlation in the case of Abell 3667 even after masking the statistically significant regions of the mass distribution.

The Offset between the cD and the centroid of mass: After analysing the data in many different ways, with different parameter sets and in different bands we concluded that the offset between the cD and the mass centroid was a real feature even though the magnitude of the offset varies from map to map. Qualitatively, the cD is to the south (and a little west) of the mass centroid in most mass plots. It is more likely to be associated with the southern (and less massive) mass component of the central double.

We used Method 2 to quantify the magnitude and significance of this offset. The best way for measuring the significance of the offset would have been to use an independent parametric model for the mass distribution and a parametric bootstrap method to generate a large number of mass reconstructions with different noise realisations and then measure the dispersion of the cD–mass centroid offset. Since such a model was not available we used the reconstructed mass map itself as the model. Combining

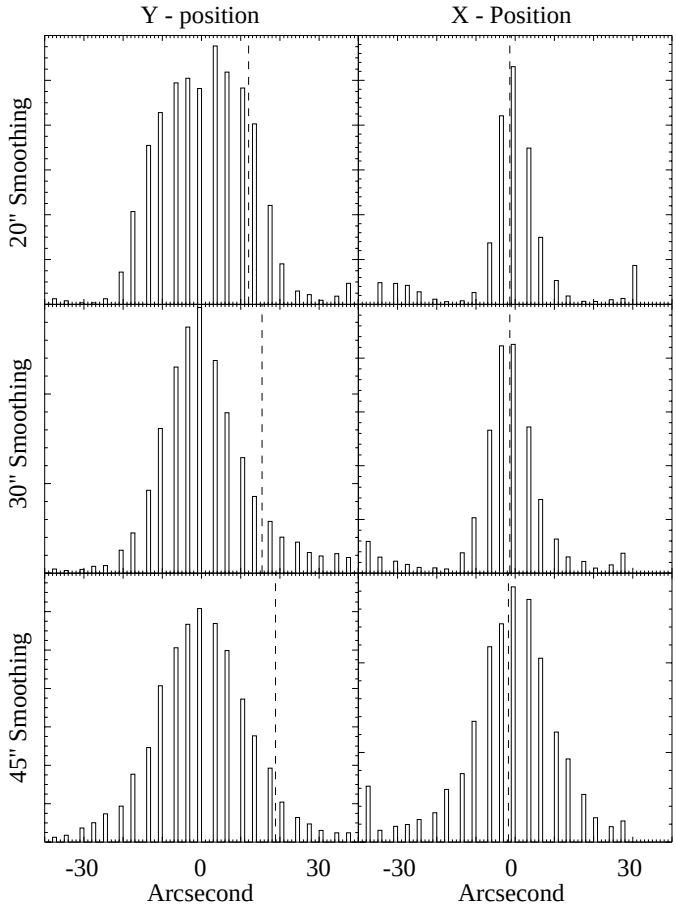

Fig. 11. Probability histograms of the location of the mass centroid obtained from parametric bootstrap resampling of the I-band shear data. The left hand plots correspond to the Y-axis offset and the right hand plots to the X-axis offset. The vertical dashed line indicates the position of the cD galaxy dashed line. The results have been plotted for 3 different smoothing scales. Note that in each plot the zero of the mass centroid is its average position; thus the cD is at different locations in each plot. Note also that the vertical scale is different for each plot (only the relative height of the bars within plot is relavant).

Table 2. The probabilities that the cD galaxy is offset from the mass centroid by more than 5 and 10 arcsec.

	$R_{\rm g} = 20''$		$R_{\rm g} = 30''$		$R_{\rm g} = 45''$	
	$\delta X_{\rm c}$	$\delta Y_{\rm c}$	$\delta X_{\rm c}$	$\delta Y_{\rm c}$	$\delta X_{\rm c}$	$\delta Y_{\rm c}$
Prob($\delta > 5''$)	0.46	0.79	0.44	0.86	0.64	0.92
Prob($\delta > 10''$)	0.21	0.48	0.20	0.68	0.30	0.73

different realisations of the noise (using the noise model of Eq. (2)), galaxy positions and intrinsic ellipticities we generated 5000 simulated datasets based on the I-band data at three different smoothing scales of 20, 30 and 40 arcsec. Figure 11 illustrates the positional stability one may expect in mass reconstructions and the numbers in Table 2 quantify the statistical significance of the offset.

Clearly, mass features move around on scales of ∼10 arcsec and this effect, naturally, increases with decrease of smoothing scale. One of the lessons we draw from this analysis is that squeezing finer mass details from the shear data is possible but at the expense of considerable flakiness in the positions of the features. It is important to reconstruct mass maps using various smoothing scales before attempting an interpretation of the same. Finally, the cD galaxy is offset to the south of the mass centroid by $19^{+22.5}_{-18.5}$ arcsec (confidence level, CL = 90%); or, the cD is at least 5 arcsec (CL = 90%) south of the mass centroid.

4.1.3. Mass profile from tangential shear

The mass from weak shear, $M_{\rm shear}$, may be obtained from Aperture Mass Densitometry or the ζ-statistics described by Fahlman et al. (1994) and Squires & Kaiser (1996). In brief, the average tangential shear in an annulus is a measure of the average density contrast between the annulus and the region interior to it; i.e. the average convergence κ ($\equiv\Sigma/\Sigma_{\rm cr}$), the ratio of the surface mass density to the critical surface mass density for lensing, as a function of the radial distance θ is given by

$$\kappa\left(<\theta_1\right) \;=\; \kappa\left(\theta_1<\theta<\theta_2\right) + \frac{2}{1-\left(\frac{\theta_1}{\theta_2}\right)^2}\int_{\theta_1}^{\theta_2}\langle\gamma_{\rm t}(\theta)\rangle\,{\rm d}\left(\ln\theta\right), \qquad (3)$$

where, $\gamma_{\rm t} = -(\gamma_1\cos 2\psi + \gamma_2\sin 2\psi)$ is the tangential component of the shear with ψ being the angle between the position vector of the object and the x-axis (RA-axis). The quantity $\langle\gamma_{\rm r}\rangle = -\langle-\gamma_2\cos 2\psi + \gamma_1\sin 2\psi\rangle$ is equivalent to the tangential component of the $Curl$ of the shear field and is expected to be zero around any closed loop in the case of a shear field arising from gravitational lensing. Thus, the scatter in $\langle\gamma_{\rm r}\rangle$ is a measure of the the noise on $\langle\gamma_{\rm t}\rangle$ due to intrinsic ellipticity, measurement noise and any other error, random or otherwise, in the shear field.

From Eq. (3), one can derive the average convergence within a series of apertures of radii θ_i, $i = 1\ldots n$

$$\kappa\left(<\theta_i\right) \;=\; \kappa\left(\theta_n<\theta<\theta_b\right) + \frac{2}{1-\left(\frac{\theta_n}{\theta_b}\right)^2}\int_{\theta_n}^{\theta_b}\langle\gamma_{\rm t}\left(\theta\right)\rangle\,{\rm d}\left(\ln\theta\right) + 2\int_{\theta_i}^{\theta_n}\langle\gamma_{\rm t}\left(\theta\right)\rangle\,{\rm d}\left(\ln\theta\right), \qquad (4)$$

where, the region $[\theta_n, \theta_b]$ is the boundary annulus which provides the reference density (the first term) in excess of which the interior density values are obtained. Thus this method provides only a lower limit to the lensing mass estimate. It is to be noted that this expression has been cast such that the first term, which cannot be calculated and hence has to be neglected, is the average within the annulus $[\theta_n, \theta_b]$ and not the average density interior to θ_b. Therefore, the effect of neglecting this term will be quite

small if the data extend sufficiently far from the cluster centre. The mass within an aperture is given by

$$M(<\theta_i) = \kappa(<\theta_i)\ \Sigma_{\rm cr}\cdot\pi\,(\theta_i D_{\rm ol})^2 = \kappa\,(<\theta_i)\ \theta_i^2\ \frac{c^2}{4G}\left\langle\frac{D_{\rm ls}}{D_{\rm os}D_{\rm ol}}\right\rangle^{-1} \quad (5)$$

where D is the angular size distance and its subscripts, l, o, and s, refer, respectively, to the lensing cluster ($z = 0.3062$), observer ($z = 0$) and the background lensed sources ($z = z_{\rm s}$). As has been explained earlier this FORS1+ISAAC dataset allowed us to estimate photometric redshifts of sources in the ISAAC field. We assumed that the 356 objects in the ISAAC field with $22.5 < R < 26.5$ and good $z_{\rm phot}$ estimates (i.e. *hyperz* fits with $\chi^2 < 1$) were representative of the FORS1 field as a whole. Of these, 302 lay behind the cluster at $z > 0.31$. From this redshift distribution we estimated $\left\langle\frac{D_{\rm ls}}{D_{\rm os}D_{\rm ol}}\right\rangle^{-1} = 1.38\pm0.03$ Gpc (1σ error). This value also includes a correction for the dilution of the lensing signal due to foreground objects being in the selected magnitude range. The mass is therefore given by

$$M(<\theta_i) = 6.14\times10^{14}\ h^{-1}\ M_\odot\ \kappa(<\theta_i)\ \theta_i'^2, \quad (6)$$

where θ_i' is in arcmin. The fractional error on the mass estimate may be obtained by adding in quadrature the fractional errors in the distance modulus and κ. The latter is much larger but we may have underestimated the former. The uncertainty quoted for the distance modulus is simply the formal error on the mean of the distribution. To this must be added the (unknown) effect of stellar contamination at the fainter levels which would underestimate the mass (presumably small – see Griffiths 1994 and Conti 1999), biases in the photometric distribution (also small, as discussed previously), source clustering and cosmic variance. However, some of the effect of the latter two must have manifested in the noise on κ.

The radial profile of the shear is shown in Fig. 12. The profile was determined in annuli centered on the mass centroid. The centre and the annuli, spaced 0.′4 apart, are marked on the bottom-left panel of Fig. 8 for reference. The annulus between 3.′2 and 3.′6 (560–635 h^{-1} kpc from the mass centroid) was used as the boundary strip to set the zero of the density scale. The filled and the open circles represent the shear ($\langle\gamma_{\rm t}\rangle$) and the *Curl* of the shear field ($\langle\gamma_{\rm r}\rangle$), respectively. The $\langle\gamma_{\rm r}\rangle$ values are indeed consistent with a zero value as expected for a lensing signal. Further, we confirmed that the error estimated for the individual shear values and used in the weighting was appropriate by checking that $\sqrt{\langle\gamma_{\rm r}^2\rangle/N} \simeq (\Sigma_1^N 1/(\delta\gamma_{\rm r})^2)^{-1} \simeq (\Sigma_1^N 1/(\delta\gamma_{\rm t})^2)^{-1}$, where N is the total number of lensed galaxies in the shell.

The mass profile inferred from the shear is shown in Fig. 13 as a series of filled circles along with the error bars. It must be noted that the shear value (Fig. 12) does not fall to zero even at the largest radii which suggests that we may be underestimating the mass of this cluster. Also it must be noted that each data point in the mass profile contains the contribution from every other point farther out and so they are not independent.

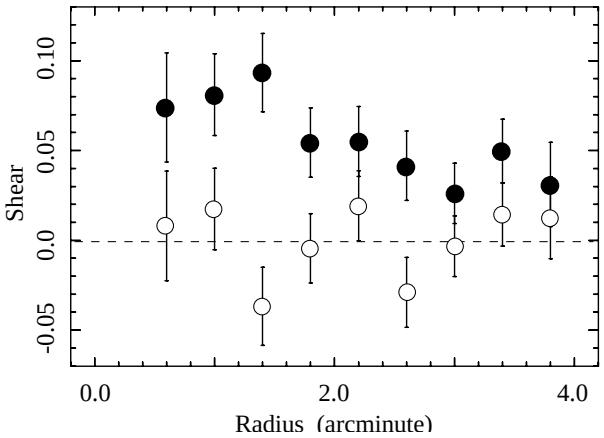

Fig. 12. Radial profile of shear in the MS 1008–1224 field. The filled circles are the tangential shear in successive annuli centered on the mass centroid (see Fig. 8). The open circles represent the *Curl* of the shear field which are expected to be (and are) distributed around zero if the shear field was due to gravitational lensing. The bars respresent $\pm1\sigma$ errors.

4.2. Magnification bias and radial depletion

The combined effect of deflection and magnification of light, results in a modification of the number density of galaxies seen through the lensing cluster. In the case of a circular lens, the galaxy count at a radius θ is

$$N(<m,\theta) = N_0(<m)\mu(\theta)^{2.5\alpha-1}, \quad (7)$$

where α is the intrinsic slope (without lensing) of the galaxy counts, μ the gravitational magnification, and N_0 the intrinsic galaxy number density (hereafter, the zero-point). Depending on the value of α, we may observe an increase or a decrease in the number of galaxies in the central region out to a limiting radius which depends on the shape of the gravitational potential and the redshift distribution of the background sources. The magnification bias has already been observed in some lensing clusters (Broadhurst et al. 1995; Fort et al. 1996; Taylor et al. 1998; Broadhurst 1998). It is particularly obvious in very deep observations as the slope of galaxy counts decreases to values as low as $\alpha \approx 0.2$ at faint levels.

4.2.1. Evidence of depletion of lensed sources

We considered as foreground those galaxies at $z_{\rm phot} < 0.25$ and as background (lensed) those at $z_{\rm phot} > 0.4$ (see Sect. 3.2). We minimized misclassification by considering only those which had a good photometric redshift solution (*hyperz* fit $\chi^2 < 1$). To be consistent with the shear analysis, we considered only the $22.5 \le R \le 26.5$ (method 1) and $22.5 \le I \le 25.5$ (method 2) samples. The galaxy counts slopes for the 2 samples were found to be 0.192

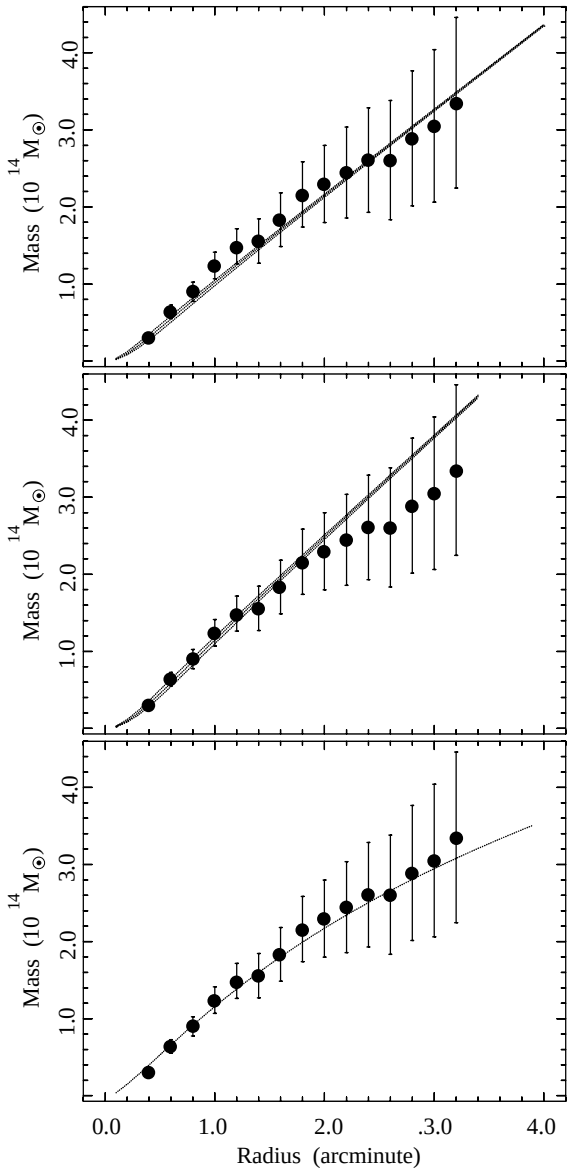

Fig. 13. The mass profile from gravitational shear analysis in MS 1008–1224. The filled circles and the error bars (1σ) in each circle represents the inferred mass profile (from R-band data). The error bar is similar to the size of the circle in the first 2 data points. The superposed curves represent mass profiles of: top panel – Pseudo-Isothermal sphere (PIS) models with a velocity dispersion $\sigma_\infty = 925$ km s^{-1} and core radii of 0.′3, 0.′4 and 0.′5; middle panel: PIS models with $\sigma_\infty = 1000$ km s^{-1} and core radii of 0.′4, 0.′5 and 0.′6; bottom panel: NFW model with $r_s = 140\ h^{-1}$ kpc and $\delta_c = 3.52 \times 10^4$. The NFW curve is a fit to the data while the others are merely illustrative in nature. See the text (Sect. 5) for a discussion of these models.

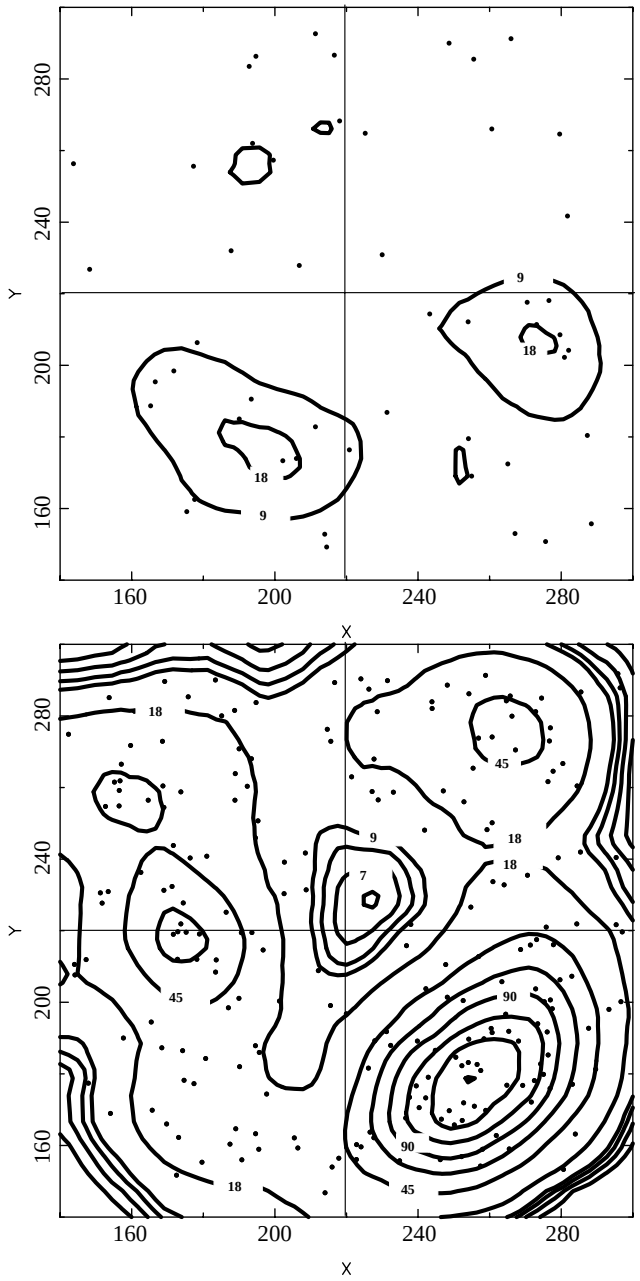

Fig. 14. Galaxy distribution in the ISAAC field (X and Y are in arcsec with north to the top and east to the left). Each point on the plot represents the location of a galaxy from the photometric redshift sample ($22.5 < I < 25.5$ and $\chi^2(z_{\rm phot}) < 1$)). The contours represent the galaxy number density field (smoothed with a 10″ Gaussian) in units of gal arcmin^{-2}. Foreground galaxies ($z < 0.25$) are plotted in the top panel. The average number density is 8 gal arcmin^{-2}. The bottom panel represents the background (lensed) galaxies ($z > 0.4$). The density averaged over the field is 36 gal arcmin^{-2}. The lowest density is close to the centre where it drops to 4 gal arcmin^{-2}. The density peaks at 180 gal arcmin^{-2}. The cross-wire marks the position of the cD galaxy. The distribution of foreground objects is, as expected, almost uniform. In contrast, the central depletion is clearly visible in the lensed galaxies. The centre of depletion is offset 7″ west and 9″ north of the cD. Also seen is the excess of galaxies in the south-west quadrant (quadrant $Q4$), which appears to be a cluster of galaxies at $z \sim 0.9$ lensed by MS 1008–1224.

and 0.233, respectively, suggesting that depletion would be significant in the FORS1 and ISAAC data.

Figure 14 shows the projected number density of galaxies having good photometric redshifts from $BVRIJK$ data and in the magnitude range $22.5 \leq I \leq 25.5$. Galaxies at $z > 0.4$ (background, lensed) are at the bottom. The control sample of foreground galaxies ($z < 0.25$) is plotted on top. In both cases, the density was corrected for the areas

masked by bright galaxies. The foreground distribution is essentially random; in contrast, a strongly depleted area is visible near the centre of the field in the background distribution. This is the first evidence of the magnification bias effect based on a large sample of background galaxies with a known redshift distribution. The cross-wire marks the location of the cD galaxy. The offset of the cD (∼10 arcsec south and 7 arcsec east) from the centre of depletion is consistent with the result from the shear analysis. The depletion and its offset from the cD are also seen in the R-selected sample.

4.2.2. Mass profile from magnification bias

The modification of the radial distribution of galaxy counts (i.e., the magnification bias) probes the amplitude of the projected mass density. In the weak lensing regime the relation simplifies to:

$$N(<m,\theta) = N_0(<m)\mu(\theta)^{2.5\alpha-1} \quad (8)$$

$$\approx N_0(<m)\left[1+2\kappa\left(\theta\right)\right]^{2.5\alpha-1}. \quad (9)$$

The mass inside a radius θ (arcmin) is given by:

$$M(\theta) = 4.4\times10^{14}\ h^{-1}\ M_\odot \left\langle\frac{D_{\rm ls}}{D_{\rm os}}\right\rangle^{-1} \times\left(\frac{D_{\rm ol}}{1\ {\rm Gpc}}\right)\int_0^\theta \theta\kappa(\theta){\rm d}\theta. \quad (10)$$

The slope of the galaxy counts, α, and the depletion curves, can be be estimated directly from the data. The quantity $\langle D_{\rm ls}/D_{\rm os}\rangle^{-1}$ may be computed from the redshift distribution shown in Fig. 4. So, in principle, one can get $\kappa(\theta)$ and hence the radial mass distribution by merely counting galaxies on the FORS1/ISAAC images but in practice we could not determine the zero-point, N_0, satisfactorily due to two reasons:

(i) The depletion extends beyond the ISAAC field.

(ii) A lensed background cluster: we detected a significant enhancement of galaxy number density on the bottom-right (hereafter Q_4) quadrant of the ISAAC field (Fig. 14, lower panel). A visual inspection of the FORS1 images showed faint and distorted galaxies between a radius of 50 and 80 arcsec from the centre of depletion. We compared the photometric redshift distribution of galaxies in Q_4 with that from the other three quadrants (Q_{1-3}). The difference between the (area-normalised) galaxy numbers in Q_4 and Q_{1-3} are plotted in Fig. 15. It shows a significant excess of galaxies at redshift 0.9. Quantitatively, in the magnitude range $22.5 \le I \le 25.5$, the number of galaxies at $z_{\rm phot} = 0.8{-}1.1$ is 61 in Q_4, whereas the three other quadrants together have 38 galaxies in the same redshift range, i.e., a $\sim6\sigma$ excess. We conclude therefore that there is a distant cluster of galaxies behind MS 1008–1224 at $z \approx 0.9$. Remarkably, the smoothed number density contours are distorted in a manner similar to the average shear pattern of galaxies at that location, as if the background cluster itself has been globally magnified and sheared. This is the first case of cluster-cluster lensing known. However, it has the unfortunate consequence of "spuriously" deepening the MS 1008–1224 radial depletion profile.

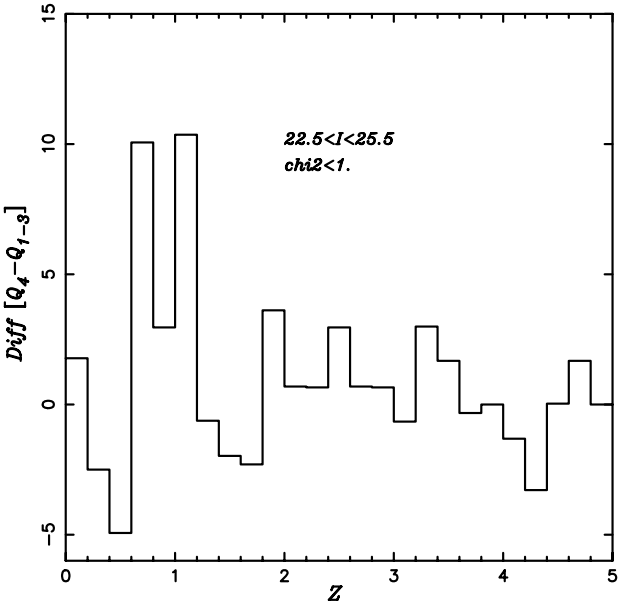

Fig. 15. A comparison of the the redshift distribution of galaxies in the South-West quadrant (Q_4) and the other 3 quadrants combined (Q_{1-3}). The difference in the galaxy numbers have been plotted after normalising the numbers by the respective areas. An excess of galaxies is seen at redshift 0.9 at a 6σ significance level. We conclude that a distant cluster of galaxies lies at this location and redshift.

So we tried to determine the asymptotic zero-point for ISAAC by extrapolating from the FORS1 field as a whole. We selected galaxies from the FORS1 field which were fainter than the brightest cluster members and outside the cluster sequence on the Colour-Magnitude plot. We then computed the radial galaxy number density from the FORS1 data within the ISAAC area, excluding the the background cluster. Figure 16 shows the depletion curves for the FORS1 field as well as for the ISAAC subsamples with photometric redshifts. A central depletion as well as a flat distribution at large distance ($N_0^{\rm FORS}$, which includes all $22.5 \le I \le 25.5$ galaxies, irrespective of redshift) beyond the extent of the ISAAC field are visible.

$$N^{\rm FORS} = N_0^{{\rm FORS}(z>0.4)}\mu^{2.5\alpha-1} + F_{\rm fg} \quad (11)$$

where $F_{\rm fg}$ is the density of unlensed galaxies (foreground galaxies plus perhaps a few cluster members) and $N_0^{{\rm FORS}(z>0.4)}$ is the zero point of the lensed background galaxies at $z > 0.4$ in the FORS1 field. A rough estimate of $F_{\rm fg} \approx 9$ gal arcmin^{-2} is obtained from the intercept of the FORS1 radial curve on the vertical axis. At large distances, the magnification is negligible, i.e. $\mu = 1$, and $N^{\rm FORS}$ is the same as $N_0^{\rm FORS}$. Using these in Eq. (11), we obtain $N_0^{{\rm FORS}(z>0.4)} = 40 \pm 6.5$ gal arcmin^{-2} (CL = 90%)

For the $z_{\rm phot} > 0.4$ sample in the ISAAC field we have

$$N^{{\rm ISAAC}(z_{\rm p}>0.4)} = N_0^{{\rm ISAAC}(z_{\rm p}>0.4)}\mu^{2.5\alpha-1}. \quad (12)$$

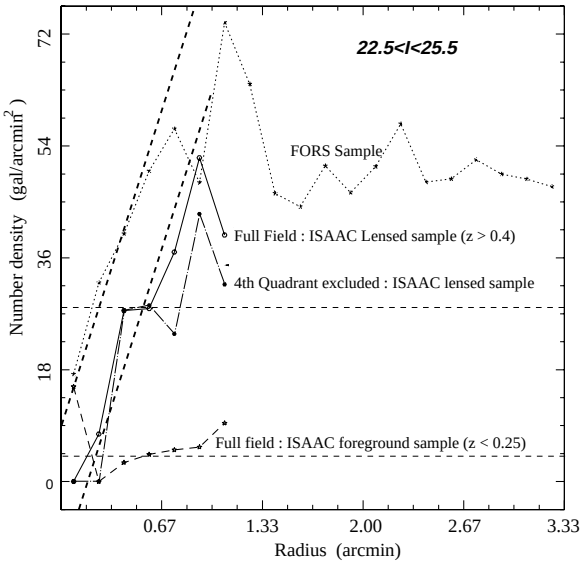

Fig. 16. Galaxy number density as function of the radial distance from the centre of depletion. All the curves are for the $22.5 < I < 25.5$ galaxy sample. The flat level in the FORS1 curve at large radius provided the zero-point for the full sample. The other curves were computed from galaxies inside the ISAAC field having a good photometric redshift. The thick dashed curves are straight line fits to the FORS1 and ISAAC samples in the inner regions and were used to calculate the fraction of ISAAC lensed galaxies with a good photometric redshift (see text).

But

$$N_0^{\mathrm{ISAAC}(z_\mathrm{p}>0.4)} = k\ N_0^{\mathrm{FORS}(z>0.4)} \tag{13}$$

where k is the (unknown) fraction of $z > 0.4$ galaxies which have been identified as such using photometric redshifts. So k is the key to determining mass from the depletion analysis. From Eqs. (11) and (13) we find

$$k = \frac{N^{\mathrm{ISAAC}(z>0.4)}}{N^{\mathrm{FORS}} - F_{\mathrm{fg}}}. \tag{14}$$

k is simply the ratio of the depletion curves for the (foreground subtracted) FORS1 and z_{phot} samples. This ratio fluctuates considerably due to Poisson noise and clustering. As a first approximation we fit straight lines to segments of the depletion curves inside 0.′67 (to exclude the background cluster) and derived an average value of $< k > = 0.65 \pm 0.17$, a zero-point of 26 ± 8 gal arcmin^{-2} for the $z_{\mathrm{phot}} > 0.4$ sample and finally a rather uncertain mass estimate of $6.6 \pm 2.2 \times 10^{14}\ h^{-1}\, M_\odot$ (CL = 90% for all) within 1 arcmin radius which is much larger than the X-ray and weak shear estimates.

In conclusion, despite the very good data set this method is still saddled with large errors. Depletion analysis is in principle very simple (just counting galaxies) and a neat way of avoiding the mass sheet degeneracy of shear analysis but is plagued by cosmic variance, background clustering and, as we have demonstrated here, the necessity of having complete redshift samples.

5. Discussion

We compared our results with X-ray and virial analyses. From Fig. 4 of Lewis et al., we see that within $175\ h^{-1}$ kpc (1 arcmin) radius the mass inferred from X-ray emissivity is $M_{\mathrm{X}} \approx 6. \times 10^{13}\ h^{-1}\ M_\odot$ which is a factor of 2 lower than the minimum estimate from our shear analysis, $M_{\mathrm{shear}} = 1.24 \pm 0.28 \times 10^{14}\ h^{-1}\, M_\odot$ (CL = 90%).

The agreement is better on larger scales. Both estimates increase monotonically and reach $M_{\mathrm{X}} = 1.82^{+0.34}_{-0.23} \times 10^{14}\ h^{-1}\, M_\odot$ and a lower limit of $M_{\mathrm{shear}} = 2.3^{+0.8}_{-0.8} \times 10^{14}\ h^{-1}\, M_\odot$ (CL = 90%) at $r = 350\ h^{-1}$ kpc (2 arcmin). At that radius, which is the limiting distance to which the X-ray data are reliable, the relative discrepancy of ∼20% is within the errors. However, even if we assume that the 20% difference is real and constant beyond $r = 350\ h^{-1}$ kpc, the baryon fraction only changes from $f_{\mathrm{b}} = 0.18$ quoted by Lewis et al. (1999) to $f_{\mathrm{b}} = 0.14$.

We compared the mass profile inferred from the shear analysis to several model mass profiles. These model curves have been plotted on the observed mass profile in Fig. 13. We note that the tightest constraint on the profiles occur at small radii. The error bars are too large to really discriminate between the models at large radii. For this reason and others described below we have plotted several models on the data and discussed them in some detail.

One drawback is the marginal detection ($+1.3\sigma$) of shear in the outermost annulus. It may just be random fluctuation – sections of this annulus lie outside the image or on the masks and so it contains fewer galaxies than it otherwise would have; indeed its error-bar is a third again as much as that of its neighbour. On the other hand, this is perhaps an indication that the mass extends out beyond the edge of the field. If so, we will have a radius dependence to the mass underestimation ($\propto R^2$) which is not expected to be significant at small radii but could be considerable at the outer points. However, we note that our models, which are basically constrained by the inner points, are not very different from the observed profile at large radii. So unless profiles in the real Universe are very different from those plotted in Fig. 13 the total mass (including the "missed" fraction) should lie within the upper limits of the present error-bars. The second problem is the presence of the background cluster described previously in the depletion analysis. Clearly, its (unknown) contribution to the projected mass density, at ∼1 arcmin from the mass centroid, has to be subtracted before fitting a model profile.

In the upper two panels of Fig. 13 we have plotted Pseudo-isothermal sphere (PIS) models on the observed profile. For $z_{\mathrm{lens}} = 0.306$ the PIS profile is given by:

$$M(r) = 1.28 \times 10^{14}\ h^{-1}\, M_\odot \left(\frac{\sigma_\infty}{1000}\right)^2 \left(\frac{r_{\mathrm{c}}}{1'}\right) \frac{x^2}{\sqrt{1+x^2}} \tag{15}$$

where r_{c} is expressed in arc-minutes, $x = r/r_{\mathrm{c}}$, $M(r)$ the mass within radius r and σ_∞ the three-dimension velocity dispersion at infinity. Each panel contains 3 curves

with the same velocity dispersion (top: 925 km s^{-1}; middle: 1000 km s^{-1}) but different core radii. The core radius values (top: 53, 70 and 88 h^{-1} kpc; middle: 70, 88 and 106 h^{-1} kpc) were selected to span the extent of the errorbar on the innermost data point where the effect of the core radius is expected to be most significant; indeed the convergence of the 3 models at large radii shows that core radius values have very little effect there. In the top panel (σ_∞ = 925 km s^{-1}) the models follow the data at large radii and we see a hint of the expected background excess at 1 arcmin. On the otherhand the σ_∞ = 1000 km s^{-1} models (middle panel) follow the inner mass points but lies above the observed profile in the outer regions; this may be a more appropriate model if we have underestimated the mass at large radii as discussed before. In general we could not fit both the rapid rise at low radii and the flatter profile at large radii satisfactorily with the same set of parameters. Thus depending on the magnitude of the correction to be applied to the observed profile we estimate a velocity dispersion of σ_∞ = 925–1000 km s^{-1}. More generally, one may cover the space occupied by the 1σ errorbars using $870 < \sigma_\infty < 1010$ and $40 < r_c < 110\ h^{-1}$ kpc (lower σ_∞ with smaller r_c). The presence of strong-lensing features also indicates a small core radius.

Carlberg et al. (1996) measured $\sigma_\infty = 1054 \pm 104$ km s^{-1} and our estimate, though somewhat smaller, is consistent with theirs. Their velocity dispersions (of MS 1008–1224 and other clusters) were in general considerably less than previous estimates. The agreement between our value and theirs suggests that their algorithm and prescriptions were reliable.

The universal profile (NFW) has been plotted on the observed profile in the bottom panel of Fig. 13. The NFW profile may be expressed for this cluster as:

$$M(x) = 1. \times 10^{10}\ h^{-1}\, M_\odot \left(\frac{r_s}{1'}\right)^3 \delta_c\ m(x) \qquad (16)$$

where $x = r/r_s$, $m(x)$ is the dimensionless mass profile (Bartelmann 1996) and $\delta_c = \rho_s/\rho_c$, where ρ_c is the critical density. The best fit gives $r_s = 140^{+212}_{-52}\ h^{-1}$ kpc and $\delta_c = 3.52^{+5.0}_{-2.9} \times 10^4$ (CL = 90%). The error bars are too large for any definitive statement and it may be meaningful to talk of a model only for the average profile from many clusters.

Figure 17 shows the radial luminosity profile of cluster galaxies selected from the Colour-Magnitude plot. The luminosity was computed assuming a no-evolution model and a K-correction appropriate for elliptical/S0 galaxies. This is reasonable since galaxies selected from the cluster sequence on a Colour-Magnitude diagram are mainly early-type systems comprising the brightest galaxies which contribute most of the luminosity of the cluster. The z = 0.31 K-correction value of 0.23 was obtained from the most recent Bruzual & Charlot (1993) models in I-band filter. At these magnitudes photometric errors were much larger than photon noise and so we assumed a constant error of δ_I = 0.1 for all galaxies. This conservative estimate made allowance for the underestimation of the K-correction for late-type galaxies of the sample.

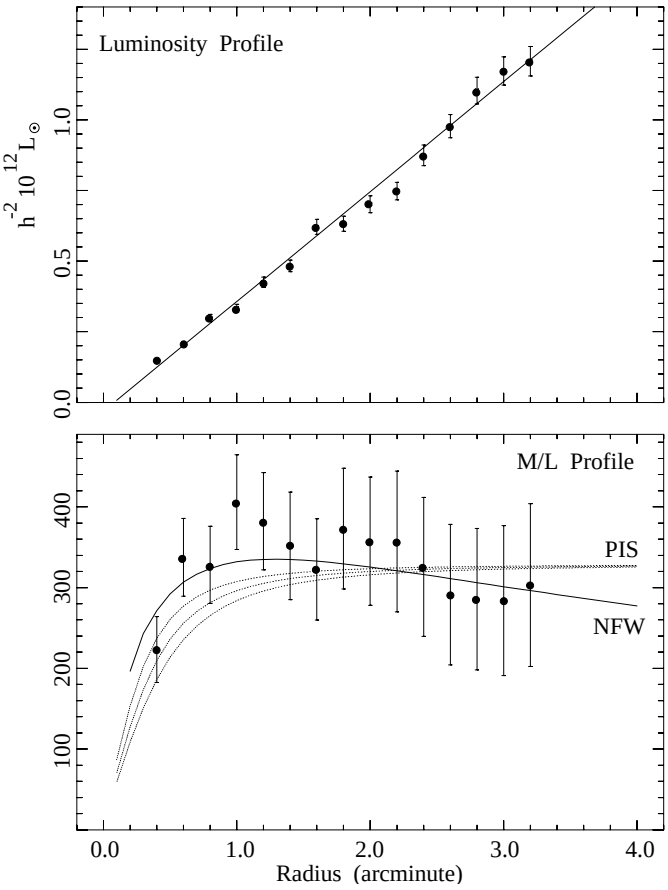

Fig. 17. Top panel: radial distribution of the total I-band luminosity of MS 1008–1224 galaxies located on the cluster sequence on the Colour-Magnitude plot. The solid line is the best fit straight line (see Sect. 5). Bottom panel: the observed Mass-to-Light ratio profile of MS 1008–1224 determined from weak-lensing mass and I-band luminosity (note: the M/L value scales with the Hubble factor h). The curves are model mass profiles divided by the linear fit to the observed luminosity profile : the solid line represents the NFW model plotted in bottom panel of Fig. 13 while the dotted lines represent the PIS models in the middle panel of 13 (lower core radius values make for flatter curves at small radii). The vertical bars represent 1σ errors.

The light profile is remarkably linear. Hoesktra et al. (1998) found similar results for Cl1358+62. The best fit to the profile gave a slope of $3.89 \pm 0.09 \times 10^{11}\ h^{-1} L_{\odot I}$/arcmin and a y-intercept of $-0.032 \pm 0.029 \times 10^{12}\ h^{-2}\, L_{\odot I}$ (CL = 90%) which is consistent with zero.

The radial profile of the mass-to-light ratio, M/L, is also shown in Fig. 17. At $r = 350\ h^{-1}$ kpc (2 arcmin) from the cluster center, $(M/L)_I = (360 \pm 80)h$. Extrapolating the outermost data points provides a value of $(M/L)_I \sim 290\ h \pm 80$ at $r = 700\ h^{-1}$ kpc (4 arcmin). This value must be scaled to a value appropriate for the r-band used in Carlberg et al. We find that our equivalent estimate of $(M/L)_r \approx 340 \pm 80\ h$ is in good agreement with the value

of $((M/L)_r = 312 \pm 84\ h$ from the CNOC analysis (all errors 1σ).

There is not much additional information (beyond that provided by the mass profile) to be had by fitting model profiles to this quantity. However, this plot brings out in a more obvious way the points we made when discussing the mass profile. The NFW model provides a better fit to the M/L profile than the PIS models because for a linear luminosity profile the M/L for the NFW model has the functional form $\mathrm{Log}(x)/x$ which has a maximum at some intermediate point. The strong constraint exercised by the innermost data point on the allowed core-radius values (PIS models : 40–110 h^{-1} kpc) and the excess of mass on intermediate scales (for both NFW and PIS models) are also seen more clearly.

The origin of this excess at 1 arcmin radius may be due to the second cluster at $z = 0.9$ which increases the gravitational amplification and shear of galaxies at $z > 1$ and located within 1 arcmin of the mass centroid. From the depletion point of view the most distant galaxies are deflected twice which increases the depth and the angular size of the depleted area. From the gravitational shear point of view, the increase in distortion due to the second cluster could have been mistakenly ascribed to the stronger gravitational potential of MS 1008–1224. This could explain why the mass from the weak lensing analysis, and therefore the radial distribution of the mass-to-light ratio shown in Fig. 17, increases rapidly at small radii ($r < 1$ arcmin) despite a linear increase of the cluster luminosity. A similar effect is also discernable in the depletion which has a very steep growth curve.

The discrepancy between X-ray and lensing mass only appears on small scales. Also with our weak-lensing mass estimate it is only a factor of 2 which is significantly lower than the factor 3.7 obtained by Wu & Fang (1997) from the analysis of strong lensing features. The decrease of the discrepancy with radius seems to be a general trend which has already been reported (Athreya et al. 1999; Lewis 1999, see Mellier 1999 and references therein). It must be noted that in most of the studies reporting a discrepancy the comparison has been done between X-ray and strong-lensing (not weak-lensing) analyses.

Some of the discrepancy observed in MS 1008-1224 can be produced by the distant cluster behind it. However, such a projection effect, similar to those discussed by Reblinsky & Bartelmann (1999), cannot explain the factor of 2 discrepancy because (i) the distant cluster occupies only a small fraction of the lensed area (1 quadrant of the ISAAC field) and (ii) only background galaxies at $z > 0.9$ are magnified twice. An upper limit to the magnitude of its impact on the mass estimate is roughly the ratio

$$\frac{1}{4}\ \frac{\left\langle \frac{D_{\rm ls}}{D_{\rm os}} \right\rangle^{-1}_{z_{\rm l}=0.9}}{\left\langle \frac{D_{\rm ls}}{D_{\rm os}} \right\rangle^{-1}_{z_{\rm l}=0.3}} \times \frac{n_{z>0.9}}{n_{z>0.3}}, \qquad (17)$$

where $n_{z>z_{\rm l}}$ is the fraction of lensed galaxies with redshift larger than $z_{\rm l}$ and the factor 1/4 is the fraction of the ISAAC area covered by the cluster. The photometric redshifts inferred with *hyperz* (Fig. 4) identified a large fraction of galaxies at $z > 0.9$ (∼50% of the $z > 0.4$ sample). Therefore, we estimate that the ratio in Eq. (17) is at most 30%, in agreement with the prediction of Reblinsky & Bartelmann (1999). In fact, the mass reconstructions do not show any obvious clump of mass at the location of the second cluster and so the effect due to this second lens is probably much weaker than the above upper limit.

It is worth noting that apart from this distant cluster contamination by other projection effects are not visible at the center where photometric redshifts provide a good idea of the clustering along the line of sight. The ISAAC field encompasses the region where strong lensing features are visible and where the mass estimate from lensing exceeds the X-ray prediction. We find no evidence that biases like the ones proposed by Cen (1997) or Metzler (1999) are significant in the central region.

There is compelling evidence that the center of mass does not coincide with the cD galaxy:

- Lewis et al. (1999) reported that the X-ray centroid was 15 arcsec north of the cD galaxy (no error listed);
- our mass reconstruction shows that the centroid is offset $19^{+22.5}_{-18.5}$ arcsec or alternatively at least 5 arcsec (both CL = 90%) north of the cD galaxy;
- our depletion analysis puts the mass centroid 10 arcsec north and 7 arcsec west of the cD (error could not be estimated).

Three independent techniques point to the offset in the same direction and of roughly the same magnitude which suggests that the cD is indeed located 10–20 arcsec to the south of the mass centroid. It may be associated with the lower clump seen in our high resolution mass maps.

The contours of isoluminosity and number density are clearly clumpy and extend northward of the cD galaxy, as do the contours in our mass maps and in the X-ray maps of Lewis et al. (1999) ... all pointers toward a dynamically unstable and perhaps merging system. If so, the hot gas is unlikely to be in equilibrium. A merging process produces shocks and gas flows between clumps, such as those seen in Schindler & Müller's simulations (1993) or those reported by Kneib et al. (1996) and Neumann & Böhringer (1999) in the lensing cluster A2218.

Athreya et al. (1999) reported very similar trends in Abell 370: good agreement between X-ray and weak lensing mass estimates on large scales and a factor of 2 discrepancy near the centre. A 370 is clearly composed of merging clumps and they ascribed the X-ray – lensing discrepancy to an oversimplified model of the hot gas in the inner regions. We suspect a similar case in the inner regions of MS 1008–1224. This, as suggested earlier by Miralda-Escudé & Babul (1995), explains the good agreement on large scales between the weak lensing, the X-ray and also the virial mass (see Lewis et al. 1999) and the apparent contradiction between X-ray and strong lensing.

We cannot rule out the possibility that the clumps in MS 1008–1224 are close to each other only in projection.

The lensing signal due to a collinear collection of condensates would mimic that of an equivalent projected mass density lens but the X-ray mass estimate would be considerably lower. This would be a more appropriate explanation if the lensing mass missed by this analysis because of the small field of view is considerable.

6. Conclusion

Thanks to the deep multicolour subarcsecond images obtained with FORS1 and ISAAC, it was possible to carry out a weak-lensing analysis of the galaxy cluster MS 1008–1224 in considerable detail:

- We made mass maps using data from 4 different bands and two different algorithms. The very similar structures seen in all maps confirmed that the presciptions for PSF corrections and noise weighting were appropriate and the reconstruction algorithms worked well.
- The remarkable stability seen in the reconstructions meant that systematic errors, if any, were essentially due to the fixed positions and intrinsic ellipticities of the background lensed galaxies. So parametric bootstrap simulations using a realistic model for the mass *and* noise distributions (using the data itself) allowed us to quantify the effect of those factors. In particular, we carried out a large number of simulations to determine the positional stability of mass features.
- The above analysis helped us quantify the significance of the offset seen between the cD galaxy and the mass centroid. Our shear and depletion analyses and the X-ray image from Lewis et al. (1999) all suggest an offset of 10–20 arcsec (30−60 h^{-1} kpc).
- The deep *BVRIJK* images were used to estimate the (photometric) redshifts of a representative sample of galaxies and determine the redshift distribution of the background/lensed population. This was used to scale the gravitational convergence (κ) into a mass value. We believe that this is the first time that redshifts have been used to determine this κ-to-mass scaling.
- We used the photometric redshifts to study the 3-Dim distribution of background galaxies and discovered a remarkable case of cluster-cluster lensing – another first. We identified a cluster at $z \sim 0.9$ which had been sheared and (presumably) amplified by MS 1008–1224 in the manner of the individual galaxies comprising it.
- Unfortunately, the contamination of the depletion curve by this lensed cluster partly compromised the use of the magnification bias effect to estimate the mass of the cluster independent of the weak shear analysis. This kind of clustering is an intrinsic limitation to the practical usefulness of the magnification bias which has already been emphasized by Fort et al. (1996) and Hoesktra et al. (1999).
- On a more optimistic note, MS 1008–1224 is a gravitational telescope facilitating by its amplification the study of a cluster of galaxies at $z \sim 1$. The amplification should have made more galaxies of this distant cluster observable than would have been possible otherwise. We have not dwelt on this point since it is beyond the scope of this work; a join multicolour and spectroscopic analysis of this cluster could be valuable.
- Weak-lensing technique only provides a lower limit to the lensing mass but comparison with (currently) plausible model profiles suggest that the underestimation is unlikely to be large for MS 1008–1224. On large scales, the mass inferred from weak lensing agrees with the X-ray estimate. In contrast, there is still a considerable amount of discrepancy on small scales. The clumpiness of the light distribution, the elongated shape, the X-ray emissivity, the double peak in the mass distribution and the offset between the cD galaxy and the mass centroid all indicate a dynamically unrelaxed cluster. We therefore believe that the X-ray gas is not in equilibrium in the innermost part of the cluster and this is the principal reason for the mass discrepancy which increases towards the centre.
- Further analysis of this cluster requires (i) infrared observations of the entire FORS1 field to determine the photometric redshifts of galaxies beyond 1 arcmin from the cluster center and hence a better estimate of the zero point of the depletion curve and (ii) HST images of the cluster center to model the innermost regions using strong-lensing features. The high resolution combined with photometric redshifts of arclets should make for a more accurate determination of the cluster center and the strong-lensing mass estimate.

Acknowledgements. We thank H. Hoesktra for providing his own updated version of the IMCAT software and for discussions on weak lensing. We thank also E. Bertin, T. Erben, N. Kaiser, R. Maoli, D. Pogosyan and P. Schneider for fruitful discussions. We acknowledge the helpful comments of an anonymous referee which considerably improved our presentation. We acknowledge efforts of the Science Verification Team of FORS1 and ISAAC at ESO for making available this excellent dataset to the ESO community.

The TERAPIX data center provided its computing facilities for the data reduction, the lensing analyses and the simulations. This work was supported the TMR network "Gravitational Lensing: New Constraints on Cosmology" and the Distribution of Dark Matter" of the EC under contract No. ERBFMRX-CT97-0172 and the Indo-French Centre for the Promotion of Advanced Research IFCPAR grant 1410-2.

References

Allen, S. W. 1998, MNRAS, 296, 392
Allen, S. W., Ettori, S., & Fabian, A. C. 2001, MNRAS, 324, 877
Appenzeller, I., Fricke, K., Fürtig, W., et al. 1998, The messenger 94, 1
Athreya, R., Hoekstra, H., Mellier, Y., Cuillandre, J.-C., & Narasimha, D. 1999, in Gravitational Lensing: Recent Progress and Future Goals, Boston University, July 1999, ASP Conf. Ser., ed. T. G. Brainerd, & C. S. Kochanek
Avni, Y. 1976, ApJ, 210, 642

Bahcall, N. A., Fan, X., & Cen, R. 1997, ApJ, 485, L53
Bartelmann, M. 1996, A&A, 313, 697
Bartelmann, M., Narayan, R., Seitz, S., & Schneider, P. 1996, ApJ, 464, 115
Bertin, E., & Arnouts, S. 1996, A&A, 117, 393
Böhringer, H., Tanaka, Y., Mushotzky, R. F., Ikebe, Y., & Hattori, M. 1998, A&A, 334, 789
Böhringer, H., Soucail, G., Mellier, Y., Ikebe, Y., & Schuecker, P. 2000, A&A, 353, 124
Bolzonella, M., Miralles, J. M., & Pelló, R. 2000, A&A, 363, 476
Broadhurst, T. J., Taylor, A. N., & Peacock, J. A. 1995, ApJ, 438, 49
Broadhurst, T. 1998, Proc. of the 19th Texas Symp., ed. J. Paul, T. Montmerle, & E. Aubourg
Bruzual, G., & Charlot, S. 1993, ApJ, 405, 538
Calzetti, D., Armus, L., Bohlin, R. C., et al. 2000, ApJ, 533, 682
Carlberg, R. G., Yee, H. K. C., Ellington, E., et al. 1996, ApJ, 462, 32
Cen, R. 1997, ApJ, 485, 39
Conti, A., Kennefick, J. D., Martini, P., & Osmer, P. S. 1999, AJ, 11
Fahlman, G., Kaiser, N., Squires, N., & Woods, D. 1994, ApJ, 437, 56
Fort, B., & Mellier, Y. 1994, A&AR, 5, 239
Fort, B., Mellier, Y., & Dantel-Fort, M. 1996, A&A, 321, 353
Gioia, I., & Luppino, G. 1994, ApJS, 94, 583
Griffiths, R. E., Casertano, S., Ratnatunga, K. U., et al. 1994, ApJ, 435, 19
Hogg, D. W., Cohen, J. G., Blandford, R., et al. 1998, AJ, 115, 1418
Hoekstra, H., Franx, M., Kuijken, K., & Squires, G. 1998, ApJ, 504, 636
Joffre, M., Fischer, P., Frieman, J., et al. 2000, ApJ, 534, L14
Kaiser, N. 1992, New Insight into the Universe, ed. V. J. Martínez, M. Portilla, & D. Sáez (Springer) 1992
Kaiser, N. 1995, ApJ, 439, L1
Kaiser, N., Squires, G., & Broadhurst, T. 1995, ApJ, 449, 460
Kneib, J.-P., Mellier, Y., Pelló, R., et al. 1996, A&A, 303, 27
Le Fèvre, O., Hammer, F., Angonin, M.-C., Gioia, I. M., & Luppino, G. A. 1994, ApJ, 422, L5
Lewis, A. D., Ellington, E., Morris, S. L., & Carlberg R. G. 1999, ApJ, 517, 587
Luppino, G., & Kaiser, N. 1997, ApJ, 475, 20
Madau, P. 1995, ApJ, 441, 18
Mellier, Y. 1999, ARA&A, 37, 127
Metzler, C. A., White, M., Norman, M., & Loken, C. 1999, ApJ, 520, L9
Miller, G. E., & Scalo, J. M. 1979, ApJS, 41, 513
Miralda-Escudé, J., & Babul, A. 1995, ApJ, 449, 18
Moorwood, A., Cuby, J.-G., Ballester, P., et al. 1999, The Messenger 95, 1
Mushotsky, R. F., & Scharf, C. A. 1997, ApJ, 482, L13
Navarro, J. F., Frenck, C. S., & White, S. D. M. 1995, MNRAS, 275, 720
Neumann, D. M., & Böhringer, H. 1999, ApJ, 512, 630
Pozzetti, L., Madau, P., Zamorani, G., Ferguson, H., & Bruzual, G. 1998, MNRAS, 298, 1133
Press, W. H., Teukolsky, S. A., Vetterling, W. T., & Flannery, B. P. 1992, Numerical Recipes in C (Cambridge University Press)
Reblinsky, K., & Bartelmann, M. 1999, A&A, 345, 1
Schindler, S., & Müller, E. 1993, A&A, 272, 137
Schneider, P., Ehlers, J., & Falco, E. E. 1992, Gravitational Lenses (Springer)
Smail, I., Ellis, R. S., Dressler, A., et al. 1997, ApJ, 479, 70
Squires, G., & Kaiser, N. 1996, ApJ, 473, 65
Steidel, C. C., Adelberger, K. L., Giavalisco, M., Dickinson, M., & Pettini, M. 1999, ApJ, 519, 1
Taylor, A. N., Dye, S., Broadhurst, T. J., Benítez, N., & van Kampen, E. 1998, ApJ, 501, 539
Tyson, J. A., Wenk, R. A., & Valdes, F. 1990, ApJ, 349, L1
Van Waerbeke, L. 2000, MNRAS, 313, 524
Van Waerbeke, L., Bernardeau, F., & Mellier, Y. 1999, A&A, 342, 15
Williams, R. E., Blacker, B., Dickinson, M., et al. 1996, AJ, 112, 1335
Wu, X.-P., & Fang, L. Z. 1997, ApJ, 483, 62